Neuroimmune cardiovascular interfaces control atherosclerosis

Sarajo K. Mohanta[1,2,*,§], Li Peng[3,*], Yuanfang Li[1], Shu Lu[1], Ting Sun[1], Lorenzo Carnevale[4], Marialuisa Perrotta[5], Zhe Ma[1], Benjamin Förstera[6], Karen Stanic[6], Chuankai Zhang[1], Xi Zhang[1], Piotr Szczepaniak[7], Mariaelvy Bianchini[1], Borhan R. Saeed[8], Raimondo Carnevale[4], Desheng Hu[9], Richard Nosalski[10], Fabio Pallante[4], Michael Beer[11], Donato Santovito[1,2,12], Ali Ertürk[6], Thomas C. Mettenleiter[13], Barbara G. Klupp[13], Remco T. A. Megens[1,2,14], Sabine Steffens[1,2], Jaroslav Pelisek[15,16], Hans-Henning Eckstein[15], Robert Kleemann[17,18], Livia Habenicht[19], Ziad Mallat[20], Jean-Baptiste Michel[21], Jürgen Bernhagen[2,6,22], Martin Dichgans[6,22], Giuseppe D´Agostino[23], Tomasz J. Guzik[7,10], Peder S. Olofsson[24], Changjun Yin[1,2], Christian Weber[1,2,22,25,*], Giuseppe Lembo[4,5,*], Daniela Carnevale[4,5,*], and Andreas J.R. Habenicht[1,2,*,§]

[1]Institute for Cardiovascular Prevention, Ludwig-Maximilians-Universität München (LMU), Pettenkoferstr. 9, 80336 Munich; Germany;

[2]German Center for Cardiovascular Research (DZHK), partner site Munich Heart Alliance, 80336 Munich, Germany;

[3]Department of Cardiovascular Internal Medicine, Second Affiliated Hospital, Guizhou University of Traditional Chinese Medicine, Guiyang, Guizhou, China;

[4]Department of Angiocardioneurology and Translational Medicine, IRCCS Neuromed, 86077 Pozzilli, Italy;

[5]Department of Molecular Medicine, Sapienza University of Rome, 00161 Rome, Italy;

[6]Institute for Stroke and Dementia Research, Klinikum der Universität München, Ludwig-Maximilians-Universität Munich (LMU), 81377 Munich, Germany;

[7]Department of Internal and Agricultural Medicine, Jagiellonian University Collegium Medicum, 31-107, Krakow, Poland;

[8]Department of Laboratory Medicine, Institute of Biomedicine, University of Gothenburg, 41390, Gothenburg, Sweden;

[9]Helmholtz Zentrum München, Deutsches Forschungszentrum für Gesundheit und Umwelt, Marchioninistr. 25, 81377 Munich; Germany;

[10]Institute of Cardiovascular and Medical Sciences, College of Medical, Veterinary and Life Sciences, University of Glasgow, G12 8QQ Glasgow, United Kingdom;
[11]Department for Information Technology, University of Jena, Jena University Hospital, 07743 Jena, Germany;
[12]Institute for Genetic and Biomedical Research, UoS of Milan, National Research Council, Milan, Italy
[13]Institute of Molecular Virology and Cell Biology, Friedrich-Loeffler-Institut, Südufer 10, 17493 Greifswald-Insel Riems, Germany;
[14]Department of Biomedical Engineering, Cardiovascular Research Institute Maastricht (CARIM), Maastricht University, Maastricht, the Netherlands;
[15]Department for Vascular and Endovascular Surgery, Klinikum rechts der Isar, Technical University of Munich, 81675 Munich, Germany;
[16]Department of Vascular Surgery, University Hospital Zurich, 8091 Zurich, Switzerland;
[17]Department of Metabolic Health Research, The Netherlands Organization for Applied Scientific Research (TNO), 2333 CK Leiden, The Netherlands;
[18]Department of Vascular Surgery, Leiden University Medical Center, 2333 ZA Leiden (LUMC), The Netherlands;
[19]II. Medizinische Klinik und Poliklinik; Technische Universität München, Klinikum rechts der Isar, Ismaningerstr. 22, 81675 Munich, Germany;
[20]Department of Medicine, Division of Cardiovascular Medicine, University of Cambridge, Cambridge CB2 0SZ, United Kingdom;
[21]Laboratory for Vascular Translational Science, INSERM UMRS 1148, University Paris Diderot (P7), GH Bichat-Claude Bernard, 46 rue Henri Huchard, 75877 Paris, France
[22] Munich Cluster for Systems Neurology (SyNergy), 81377 Munich, Germany.
[23]Faculty of Biology, Medicine and Health, University of Manchester, Manchester, M13 9PL, United Kingdom;
[24]Laboratory of Immunobiology, Center for Bioelectronic Medicine, Department of Medicine, Solna, Karolinska Institutet, Karolinska University Hospital, 17164, Stockholm, Sweden;
[25]Department of Biochemistry, Cardiovascular Research Institute Maastricht, Maastricht University, Maastricht, the Netherlands;

[§]Corresponding authors: Sarajo K. Mohanta; Sarajo.Mohanta@med.uni-muenchen.de; Andreas J.R. Habenicht; Andreas.Habenicht@med.uni-muenchen.de;

[*]Equal authors

Atherosclerotic plaques emerge in the inner intimal layer of arteries causing heart attacks and strokes[1]. As plaques lack innervation, the impact of neuronal control on atherosclerosis remains unknown. However, the immune system responds to plaques by forming leukocyte-infiltrates in the outer connective tissue-coat of arteries, i.e. the adventitia[2-6]. Because the peripheral nervous system (PNS) uses the adventitia as its principal conduit to reach distant targets[7-9], we postulated that the PNS may directly interact with diseased arteries. Surprisingly, wide-spread neuro-immune-cardiovascular-interfaces (NICIs) arose in murine and human atherosclerosis: diseased adventitia segments showed expanded axon networks including growth cones at axon endings near immune cells and media smooth-muscle-cells. Murine NICIs established a structural artery-brain-circuit (ABC): abdominal adventitia nociceptive afferents[10-14] entered the central NS through spinal cord T_6-T_{13} dorsal root ganglia, and were traced to higher brain regions including parabrachial and central amygdala neurons; and sympathetic efferents projected from medullary and hypothalamic neurons to the adventitia through spinal intermediolateral neurons and both celiac and sympathetic chain ganglia. Moreover, ABC PNS components were activated: splenic sympathetic and celiac vagus nerve activities increased parallel to disease progression while celiac ganglionectomy led to disintegration of adventitial NICIs, reduced disease progression and enhanced plaque stability. Thus, the PNS employs NICIs to assemble a structural ABC and therapeutic intervention into the ABC attenuates atherosclerosis.

The nervous and vascular systems interact at multiple levels. During ontogeny, mutually acting guidance cues synchronize morphogenesis of the peripheral nervous system (PNS) and blood vessels[7]; in adult organisms, the central NS (CNS) and blood vessels form various blood-brain barriers[15]; and blood vessel-derived molecules regulate axon growth and angiogenesis[8,9]. These data reveal developmental and homeostatic principles shared by the cardiovascular system and the NS in physiology. Moreover, aberrant neuroimmune interactions have been identified in clinically important diseases[16].

Atherosclerosis is the major driver of cardiovascular disease and morbidity[1]. Its hallmark is the atheromatous plaque in the inner intimal layer of arteries. Plaques may impair blood supply to vital organs causing heart attacks and strokes, among other life-threatening events. The outer connective tissue coat of arteries, i.e. the lamina adventitia, is used by the NS as its principal conduit to reach peripheral tissues[7-9]. Yet, innervation in atherosclerosis has not been considered before, because plaques are not innervated. Intriguingly, however, atherosclerosis progression is paralleled by accumulation of immune cells in those adventitia segments that are adjacent to plaques but not in plaque-free segments[2]. As the disease progresses, adventitial immune cell infiltrates expand systemically in the arterial tree and some immune cell aggregates develop into well-structured artery tertiary lymphoid organs (ATLOs) at distinct sites in both mice and human arterial beds[2-5,17]. These observations together with progress in the neuroimmunology of inflammatory diseases[18-21] led us to consider the possibility that the PNS interacts with plaque-associated adventitial leukocytes. Here, we report that distinct neuroimmune cardiovascular interfaces (NICIs) emerge during atherogenesis, that they participate in the formation of an activated structural artery-brain-circuit (ABC), and that targeting the sympathetic nervous system (SNS) of the ABC participates in the control of atherosclerosis progression.

Delineation of adventitial axonogenesis

Neurofilament-200^{+} (NF200) axons and axon bundles were abundant in the adventitia of aged wild-type (WT) and apolipoprotein-E deficient (Apoe$^{-/-}$) mice (Figs.1,2; Extended

Data Figs.1-4). In WT mice, axon density was higher in the abdominal *vs* the thoracic aorta and in artery branches *vs* non-branching segments (Extended Data Figs.1a-c). Although axon density in the Apoe$^{-/-}$ adventitia without adjacent plaques was similar to that of WT adventitia, it increased in segments adjacent to atherosclerotic plaques, and plateaued in ATLOs (Fig.1a; Extended Data Figs.1b-d). Plaque sizes correlated with axon density (Extended Data Fig.1e). Axons expressed tyrosine hydroxylase (TH) or calcitonin-gene-related-peptide (CGRP), but not choline acetyl transferase (ChAT) (Fig.1b; Extended Data Fig.1m), and transient receptor potential vanilloid 1 (TRPV1)$^{+}$ axons co-expressing CGRP were found throughout the WT and Apoe$^{-/-}$ adventitia (Fig.1b). Norepinephrine tissue levels were indistinguishable in atherosclerotic plaque-free segments of Apoe$^{-/-}$- *vs* WT mice but they were higher in plaque-burdened segments (Fig.1c; Extended Data Fig.3f). Axons expressed tubulin β3 (Extended Data Fig.1f), a protein involved in axon maintenance/guidance, and growth-associated protein 43, a marker of growth-cones at axon endings (Fig.1d) indicating that the PNS responds to plaques by forming neuro-adventitia connections by directly innervating constituents of the adventitia. Expression of two presynaptic proteins, i.e. synapsin and synaptophysin[22,23], robustly increased at axon endings co-expressing neurofilament M (NFM) in Apoe$^{-/-}$ *vs* WT adventitia segments (Fig.1e; Extended Data Fig.1g) similar to TH^{+}/CGRP^{+} axon endings (Fig.1e). While NF200^{+}/NFM^{+}/TH^{+} or synapsin^{+}/synaptophysin^{+} axon endings were observed throughout the arterial tree of both WT and Apoe$^{-/-}$ mice, they frequently localized in close proximity to leukocytes (Extended Data Figs.1h-l; **video 1,2**) resembling neuro-adipocyte junctions or neuro-microglia junctions[24,25]. Moreover, synapsin^{+}/synaptophysin^{+} axon endings accumulated at the adventitia/media border in close proximity of the outer layer of media smooth muscle cells (SMCs) (Fig.1e; Extended Data Figs.1g,j; compare **videos 3,4**). Synapsin localized in the low nanometer range distance to leukocytes or SMCs (Figs.1f,g; **video 5,6**). These data indicated that sympathetic and nociceptor axon endings directly innervate the adventitia in Apoe$^{-/-}$ mice (Fig.1h).

Gene expression in the PNS

Differential neuronal gene expression profiles during aging were mined in WT *vs* Apoe$^{-/-}$ aortas and separately in WT adventitia, Apoe$^{-/-}$ adventitia without ATLOs, and Apoe$^{-/-}$ adventitia with ATLOs, and plaques[4] and in aged WT *vs* Apoe$^{-/-}$ renal lymph nodes (RLN) and spleens (http://www.ncbi.nlm.nih.gov/geo/; GSE40156; GSE94044) for numerous NS-related gene ontology terms (Extended Data Fig.2; supplementary Tables 1-5). NS genes including those involved in axon neogenesis, axon guidance, and synaptic transmission were upregulated in adult Apoe$^{-/-}$ mice and further increased in aged Apoe$^{-/-}$ mice (Extended Data Figs.2a-d). Numerous genes regulating axonogenesis were higher in adventitia segments adjacent to atherosclerotic plaques whereas axon repellants such as semaphorin 3A, 3F and 3C genes were lower (Extended Data Figs.2e-i). Moreover, neuronal gene expression of ATLOs *vs* RLNs of both genotypes showed numerous up-regulated genes (Extended Data Figs.2j,k), though WT *vs* Apoe$^{-/-}$ RLNs or spleens showed no difference (Extended Data Figs.2l,m). In line with gene expression data, we observed increased density of aldehyde dehydrogenase 1-expressing retinoic acid-secreting axons, and nerve growth factor expression in ATLOs (Extended Data Figs.2n,o). Although no ChAT-expressing axons were detectable, ChAT-expressing T and B cells were abundant in ATLOs (Extended Data Fig.1m), in RLNs and spleens (Extended Data Fig.1n). Differential expression of genes regulating other neuroimmune interactions including higher adrenergic receptor β2 (*adrβ2*) but lower *adrβ1* and *adrβ3* transcripts in ATLOs were observed (Extended Data Fig.1o). A higher percentage of CD4$^+$ T cells, CD8$^+$ T cells, and B220$^+$ B cells expressing ADRβ2 with a disproportionally higher number of effector memory T cells were observed in ATLOs *vs* RLNs or spleens (Extended Data Figs.1p-r). Thus, adventitia segments of atherosclerotic arteries harbor a distinct set of immune cell subtypes and phenotypes that differs from those in secondary lymphoid organs[4].

Axonogenesis in the arterial tree

Examination of further arterial beds (Extended Data Fig.3a) showed prominent axon neogenesis in Apoe$^{-/-}$ mice indicating that the axon neogenesis phenotype in atherosclerosis is of systemic nature affecting all arteries. To rule out an Apoe-genotype

confound, we studied Apoe-sufficient hyperlipidemic mice *vs* their normolipidemic controls. We examined axon neogenesis in RLNs and spleens, but failed to find increased axon density in Apoe$^{-/-}$ *vs* WT mice (Extended Data Fig.3b), in line with similar NS gene expression patterns (Extended Data Fig.2l,m). However, we observed higher norepinephrine levels in aged Apoe$^{-/-}$ *vs* WT spleens (Extended Data Fig.3c; see also Fig.4a below). Next, we studied axon density in the aortic root of adult low-density-lipoprotein receptor-deficient mice on a Western-type diet. We found increased densities of NF200^{+}/TH^{+}/CGRP^{+} axons adjacent to plaques (Extended Data Fig.3d), similar to adult Apoe$^{-/-}$ mice (Extended Data Fig.3e). Axon neogenesis was accompanied by enhanced norepinephrine levels in plaque-burdened aortic root segments (Extended Data Fig.3f). In addition, we studied axon density in aged humanized Apoe4-knockin mice and observed that hyperlipidemic Apoe4-knockin mice on a high-fat-diet showed higher axon densities *vs* their normolipidemic controls on standard rodent chow diet (Extended Data Fig.3g). These data indicated that adventitia innervation consists of a mixture of axon endings directly innervating the adventitia and other passing fibers directed to distant targets; that axon neogenesis is restricted to atherosclerotic segments throughout major arterial tree territories; that there is no systemic increase in axon density; and that these responses parallel disease progression. More studies, however, will be needed to characterize the subcellular structures of the axon endings as *bona fide* axon terminals.

PNS ganglia neurons innervate arteries

We next used tissue clearing to characterize the spatial relation between axons in the adventitia, the celiac ganglion (CG), and sympathetic chain ganglia (SycG). Segmentation and tracing of intact abdominal aorta after 3D imaging of solvent-cleared organs coupled with light-sheet-microscopy showed juxtaposition of the CG complex and the SycGs with their axons extending into the aorta adventitia (Fig.2a; Extended Data Fig.4a **video 7**). Robust restructuring of the nerve network emanating from the ganglia towards the adventitia was apparent in Apoe$^{-/-}$ mice (Fig.2a,b; **video 8**) for both CGs and SycGs (Fig.2a). Restructuring primarily involved small-diameter nerve fibers and their apparent varicosities[26] (Fig.2b,c; Extended Data Figs.4b,c; **videos 9,10**). Yet, axons penetrating the external lamina of the aorta into the media remained undetectable

(Extended Data Figs.4d,e; **video 11**). We next used aqueous 2,2'-thiodiethanol clearing to quantify axon bundle density: axons and axon bundles penetrating ATLOs were up to 40-fold higher in Apoe$^{-/-}$ *vs* WT mice (Fig.2d), including multiple axon endings originating from single axons in ATLOs (Fig.2e, Extended Data Fig.4f; **video 12**). Within ATLOs, axon sprouting was higher in CD3e^{+} T cell *vs* B220^{+} B cell areas reaching levels comparable to those in lymph nodes (Extended Data Fig.4g). We next examined newly formed axons *vs* mature axons using neurofilament L for newly formed immature axons and neurofilament H for mature axons as reported[27]. WT axons showed double neurofilament H^{+}/L^{+} axons but no or less single neurofilament L^{+} axons (Extended Data Fig.4h) but newly formed single neurofilament L^{+} axons were readily observed in ATLOs (Extended Data Fig.4h). Thus, the SNS undergoes restructuring in areas adjacent to atherosclerotic plaques (Fig.2f). These data raised the issue of potential cause-effect relationships regarding the atherosclerosis-related adventitia axonogenesis phenotype.

Signaling via the lymphotoxin β receptor in arterial SMCs participates in the formation of ATLOs[4] as previously shown in mice carrying an SMC-specific deletion of the lymphotoxin β receptor (Apoe$^{-/-}$/Ltbr$^{fl/fl/Tagln\text{-}cre}$). Axon density in age- and sex-matched Apoe$^{-/-}$/Ltbr$^{fl/fl/Tagln\text{-}cre}$ mice was significantly reduced *vs* Apoe$^{-/-}$ controls but was elevated *vs* WT mice[4] (Extended Data Fig.3h). These data suggest that signaling through the SMC-lymphotoxin β receptor participates in adventitial axon neogenesis.

Axonogenesis in human atherosclerosis

Critical features identified in murine artery innervation were observed in a range of human cardiovascular tissues including sex- and age-matched cases that included atherosclerosis-free coronary arteries derived from organ donors, coronary arteries from patients undergoing cardiac transplant surgery with ischemic or dilated cardiomyopathy with or without atherosclerosis; and non-aneurysmatic abdominal aortas from kidney donors and abdominal aortas from asymptomatic abdominal aortic aneurysms with or without atherosclerosis (supplementary Tables 7,8). Coronary arteries of explanted hearts showed increased densities of NF200^{+} and TH^{+} axons in plaque-burdened *vs* plaque-free or healthy artery segments (Extended Data Figs.5a,b). Pronounced regional axon neogenesis was apparent in atherosclerotic aortic aneurysms of identical surgical

specimens: densities of $NF200^+$ nerves and TH^+ sympathetic nerves were 8-10 fold higher in plaque-burdened abdominal aortic aneurysm segments *vs* plaque-free aneurysmatic adventitia or healthy aorta segments with a concomitant increase in norepinephrine levels (Extended Data Figs.5c,d); axon density was ~6 fold higher in ATLO-containing aneurysmatic segments compared to non-ATLO areas (Extended Data Fig.5e). We also observed perineural TLO-like leukocyte aggregates in diseased human cardiovascular tissues (Extended Data Figs.5f,g), infiltration of $CD45^+$ leukocytes in adventitial nerves of atherosclerotic abdominal aneurysmatic aorta *vs* unaffected segments (Extended Data Fig.5h).

Widespread inflammation in the PNS

We next examined murine larger-sized nerves, perivascular ganglia (PvaGs), and the somatosensory dorsal-root-ganglia (DRGs). Surprisingly, we found widespread inflammation in PvaGs, nerves and DRGs in aged $Apoe^{-/-}$ mice. Yet, we did not observe follicular dendritic cells in germinal centers in these adventitia-remote areas and therefore termed these leukocyte infiltrates as *tertiary lymphoid clusters* to distinguish them from ATLOs and lymph nodes (Extended Data Fig.6a). However, TH^+ sympathetic PvaG- and nerve-associated as well as DRG-associated lymphoid clusters contained immune cells and structures including macrophages, T cells, B cells and conduits very similar to ATLOs[3] (Extended Data Figs.6b-f). Tertiary lymphoid clusters in the PNS correlated with atherosclerosis in aged mice (Extended Data Fig.6g) and sizes of PvaG-lymphoid clusters correlated with both plaque- and ATLO sizes (Extended Data Figs.6h,i,o). This data indicated atherosclerosis-related widespread inflammation of nerves and ganglia and restructuring of the PNS in different regions of the vascular system during aging. We examined PvaGs using gene expression analyses of WT and $Apoe^{-/-}$ mice. Gene ontology cluster analyses revealed multiple differentially expressed immune response-related transcripts, and up-regulation of axon neogenesis-related transcripts in $Apoe^{-/-}$ PvaGs (Extended Data Figs. 6j-l, supplementary Table 6, GSE93954). All PvaGs showed SNS genes with a prominent mast cell gene signature (Extended Data Figs.6k,m; supplementary Table 6). These data showed infiltration and/or expansion in the somata of PvaGs and DRGs by macrophages, T cells, and mast cells (Extended Data Fig.6n). Mast cells had previously been identified to connect to

sensory nerve fibers in coronary artery adventitia[28,29]. Remarkably, Apoe$^{-/-}$ PvaGs showed higher expression levels of the lymphorganogenic chemokine CXC-ligand 13[4] *vs* WT PvaGs indicating a potential mechanistic link of immune cell infiltration in and/or around PNS ganglia (Extended Data Fig.6p). These data revealed that chronic inflammation in atherosclerosis extends to major components of the PNS in aged Apoe$^{-/-}$ mice.

Emergence of a structural artery brain circuit (ABC)

The body of data above raised the important possibility that components of the PNS may be hardwired to the CNS. To map connections between the adventitia and the CNS that may emerge during the development of atherosclerosis, we used a neurotropic retrograde-migrating pseudorabies virus strain (PRV-Bartha) (Extended Data Figs.7a,b). First, we injected ink[4] or PRV into ATLOs to examine the neutropic migration characteristics of the latter. While ink but not PRV appeared in the adventitia-draining RLNs (Extended Data Fig.7c), PRV-immunoreactivity (PRV-IR) was associated with axon endings within 30 minutes and thereafter post-inoculation indicating successful adventitia targeting of the virus injection (Fig.3a). Longitudinal mapping of PRV retrograde migration from the aorta adventitia showed PRV-IR in PvaG, CG and SycG at day 2 (d2) or d4 post-inoculation (Fig.3b, Extended Data Fig.7d) and in thoracic T_6-T_{13} DRGs at d4 (Fig.3c, Extended Data Fig.7e). In the CNS, PRV-IR was detected within distinct spinal cord and brain nuclei at d4, including the intermediolateral (IML) neurons in the spinal cord gray columns (Fig.3d), the medullary neurons in the raphe pallidus nucleus (RPa), the gigantocellular reticular nucleus-alpha, the lateral paragigantocellular nucleus, and the paraventricular hypothalamic nucleus (PVN) (Fig.3e,f; Extended Data Figs.7f-h). Given the selective retrograde migration characteristics of PRV, this data indicated polysynaptic brain-to-adventitia projections. Quantitative kinetic mapping of PRV^{+} neurons in specific brain nuclei over a prolonged post-inoculation time using the Allen Mouse Brain Atlas (http://mouse.brain-map.org/) and the Mouse Brain Connectivity Atlas (http://connectivity.brain-map.org/) delineated the routes of PRV migration from first order SNS neurons to next order neurons (Extended Data Figs.7f-j), indicating a larger central network including the central nucleus of the amygdala, the rostral

ventrolateral medulla, the locus coeruleus, and the dorsal motor nucleus of the vagus (10N) (Fig.3g; Extended Data Figs. 7g-i). PRV^+ neurons included $ChAT^+$ cholinergic neurons in the 10N, the RPa, and TH^+ catecholaminergic neurons in the PVN and the locus coeruleus, which are known to regulate parasympathetic and sympathetic outflows, respectively (Fig.3e,f; Extended Data Figs. 8a,d). To corroborate that PRV originating in the adventitia traces a *bona fide* adventitia brain axis, we performed additional control tracing studies by targeting the *vision circuit*, the *kidney-brain circuit*, and the *lumbar psoas major muscle-brain circuit*. PRV^+ neurons were detected in the predicted brain areas after eye, kidney and muscle injections (Extended Data Fig.7k). Comparative mapping and quantification of PRV^+ neurons following adventitia injections showed distinct connectivity features regarding the adventitia brain axis *vs* previously characterized circuits (Extended Data Figs.7k,l). Injection of the virus into the circulation did not result in infection of the PNS or the CNS up to 7d post-inoculation (Extended Data Fig.7k). While our tracing experiments revealed robust central components of a structural ABC, we did not observe PRV-IR in the 10N, a major parasympathetic central node, at early time points but at later time points (Extended Data Fig.8a). To further substantiate the veracity of this delayed PRV migration, for comparison, we also injected PRV into the greater curvature of the stomach wall, whose vagal innervation has been well characterized[30]. After injection into the stomach wall, we detected PRV-IR in the nodose ganglion at d2, the 10N at d3, and the NTS at d4 (Extended Data Fig.8b), indicating that stomach injection efficiently targeted the vagus, while after adventitia injection, the virus was not seen in the nodose ganglion and NTS neurons until d5 and until d6 for 10N. These data are best explained by the presence of additional synaptic nodes or an indirect ABC migration route between these structures and adventitia and further support a lack of direct vagal innervation of the aorta (Extended Data Figs.8a,b). In $Apoe^{-/-}$ *vs* WT mice, more PRV^+ neurons were found in distinct medullary and hypothalamic brain nuclei (Extended Data Figs.8c,d), involved in sympathetic outflow regulation. The phenomenon that PRV^+ neurons in some brain nuclei of $Apoe^{-/-}$ brains are more abundant than in WT brains may be due to the expanded axon network in the $Apoe^{-/-}$ adventitia thereby providing a larger contact surface facilitating for virus entry in $Apoe^{-/-}$ mice.

Atherosclerosis is associated with activation of distinct brain neurons

We next assessed the expression of cFos, an established neuronal activation marker. More cFos^{+} neurons were found in the IML and the ventral horns of the spinal cord; the RPa of the medulla; the PVN of the hypothalamus; the parabrachial nucleus of the pons; and the central amygdala, but not in other amygdala nuclei in Apoe$^{-/-}$ *vs* WT mice (Fig.3h-l; Extended Data Figs.8e). cFos^{+} neurons included ChAT^{+} cholinergic neurons in the spinal IML, in the medullary RPa, and the lateral paragigantocellular nucleus; TH^{+} catecholaminergic neurons in the medullary RPa, the locus coeruleus of the pons; and the CGRP^{+} neurons in the parabrachial nucleus of the pons (Figs.3h-k; Extended Data Figs.8f-h). Moreover, cFos^{+} neurons were abundant in the CGRP^{+} sensory axon-rich central nucleus of amygdala and the nucleus of the solitary tract (NTS) (Fig.3l; Extended Data Fig.8i). These data indicated activation of distinct neurons in multiple - but not all - brain nuclei in atherosclerosis (Figs. 3m,n).

The ABC is activated during aging

To further explore potential neuronal activities of components within the structurally delineated ABC, we recorded nerve activity from the splenic nerve, which originates in the CG (splenic sympathetic nerve activity, SSNA)[31,32]. SSNA in young WT *vs* Apoe$^{-/-}$ mice were identical (Fig.4a) but increased in adult Apoe$^{-/-}$ mice and remained elevated in aged Apoe$^{-/-}$ mice, as compared to aged-matched WT controls (Fig.4a; Extended Data Fig.10a). To examine a potential regulation of SSNA by the celiac branch of the vagus nerve, we surgically denervated the distal end of the nerve while concomitantly recording SSNA. Celiac vagotomy significantly reduced the number of spikes in the time window of SSNA analyzed in adult and aged Apoe$^{-/-}$ mice (Extended Data Fig.10b), indicating that the activity of SSNA partly depends on a direct modulation by the celiac vagus nerve, consistent with the concomitant elevation of celiac vagus nerve activity directly recorded in aged Apoe$^{-/-}$ mice (Fig.4b). We further found increased transcripts associated with transmission of nerve impulses in PvaGs of Apoe$^{-/-}$ *vs* WT mice that are known to control neuron activation in peripheral nerves (Extended Data Fig.10c; supplementary Table 6)[33].

ATLOs collapse following SNS denervation

Ultrasound *in vivo* imaging of the heart, aortic arch and abdominal aorta was used to estimate cardiovascular parameters and plaque volume in animals of different ages (Extended Data Fig.9a; **video 13**). These measurements yielded reliable data as plaque volume correlated with conventional postmortem quantitation of intima/media ratios (Extended Data Figs.9b-e). No significant changes in blood pressure were noticed in WT *vs* Apoe$^{-/-}$ mice though lumen diameters and β-stiffness of the aortic arch were increased in adult and aged Apoe$^{-/-}$ mice (Extended Data Figs.9f,h; supplementary Tabl.9). Moreover, heart rate variability, a proxy measure of centrally regulated integration of the sympathetic and parasympathetic NS activities remained similar across the lifespan of WT and Apoe$^{-/-}$ mice (Extended Data Fig.9g). We initially denervated the SNS using 6-hydroxydopamine (6-OHDA) in aged Apoe$^{-/-}$ mice[20] (Extended Data Fig.10d). 6-OHDA was effective in denervating the SNS in the periphery but not in the CNS as evidenced by similar TH expression in the locus coeruleus of treated and untreated mice (Extended Data Fig.10e). Moreover, 6-OHDA markedly reduced aortic and splenic norepinephrine levels or TH^{+} axon density indicating nearly complete functional ablation of sympathetic nerve endings and varicosities of the PNS (Fig.4c; Extended Data Fig.10f). Surprisingly, treatment led to a rapid collapse of ATLOs as revealed by their reduced number and size, loss of T and B cell infiltrates and elimination of ATLO structures within days (Fig.4d,e; Extended Data Figs.10g,h). The effect of 6-OHDA treatment on atherosclerosis did not reach significance within 4 weeks as expected (Fig.4e,f). 6-OHDA did not affect multiple control parameters including plasma cholesterol levels, but decreased CD150^{+}CD48^{-} hematopoietic stem cells and CD34^{+}CD16/32^{+} granulocyte-macrophage progenitors in the bone marrow; and it increased Foxp3^{+} T regulatory cells in secondary lymphoid organs and ATLOs (Extended Data Figs.10i-k) extending - to aged mice and ATLOs - data previously reported by others[34].

Celiac ganglionectomy disrupts ATLOs and attenuates atherosclerosis

To study the impact of the CG on ATLOs and atherosclerosis, celiac ganglionectomy (CGX) was performed in adult mice[35] and atherosclerosis progression was assessed during 8 months thereafter by ultrasound *in vivo* imaging (Extended Data Fig.10l). CGX reduced aortic and splenic norepinephrine levels or TH^{+} axon density indicating effective

surgery (Fig.4g; Extended Data Fig.10m). CGX mice showed unchanged plasma cholesterol levels or relative organ weights (Extended Data Fig.10n) but reduced plaque volumes (Figs.4h,i). Morphometry showed decreased numbers, sizes and cellularity of ATLOs (Figs.4j,k). CGX reduced $CD11b^+$ myeloid cells in spleen (Extended Data Fig.10o), and reduced plaque sizes along with parameters of plaque vulnerability without affecting internal diameter/β-stiffness or media area of the aorta, thus resulting in enhanced plaque stability (Figs.4k,l,n; Extended Data Figs.10p-r,t). None of the changes in nerve activities or atherosclerosis were due to alterations in hemodynamic parameters including blood pressure and heart rate variability[36] (Figs. 4m,n; Extended Data Figs.9g,h, 10s; supplementary Table 10).

Discussion

Data reported above support the conclusion that the adventitia NICIs are proxy sentinel sensors and effectors of atherosclerosis created by long-lasting interactions of the PNS with both the immune and vascular systems; the initiating event to establish a structural ABC seems to originate in plaques of diseased arteries in young mice; over time, however, a multisynaptic structural ABC emerges during adulthood and aging including a sensory arm and sympathetic and parasympathetic effector arms; and therapeutic intervention into the SNS attenuates atherosclerosis (Extended Data Fig.11).

Though neuroimmune interactions[37] have been described before including those in cancer[27], obesity[24], thermoregulation[38], brain diseases[6], and inflammatory bowel diseases[16,39], identification of the structural ABC may establish a new yet to be fully appreciated disease paradigm: It addresses multiple pathways of neuroimmunology in atherosclerosis[40] but then integrates the vascular system as a primary third systemic participant in atherosclerosis[8]. Our data suggest that the vascular system[3] qualifies for a dual role in tripartite rather than bidirectional tissue interactions in atherosclerosis: the adventitia layer acts as an indispensable scaffold for the NS by directly initiating interactions vis-à-vis the PNS and CNS, and the immune system[37,41]; while its intima layer recruits leukocytes via endothelial cells from the lumenal side to promote plaque growth[1,8]. Future studies should thoroughly explore these propositions of tripartite rather than bidirectional interactions within the adventitia NICI and delineate the impact of the

vascular system in the neuroimmunology of multiple unresolvable diseases other than atherosclerosis.

We consider the following sequence of events: adventitia NICIs appear to be initiated in arteries throughout the arterial tree[2,3,6,42,43] resulting in restructuring of the PNS wherever atherosclerotic plaques arise. Eventually, atherosclerosis-triggered inflammatory mediators or other cues generate action potentials at sensitized nocisensor-expressing adventitia axons[10-14] and this electrical activity may be conveyed via DRG neurons to the spinal cord and along the pain pathway to higher brain regions including the central amygdala[44-47]. Thus, the sensory arm of the adventitia NICI emerges as a peripheral tissue transducer of atherosclerosis capable of receiving plaque-derived molecular information via the nocisensor TRPV1 and possibly multiple other TRP channels to ultimately reach the brain[10-13,46,47]. In addition to an ABC sensor, an efferent SNS effector projects from the hypothalamus and medulla to the abdominal adventitia via the CG and the SycGs and possibly multiple additional SNS ganglia in territories of the arterial tree other than the abdominal aorta segment examined here. In addition to this structural ABC, however, efferent sympathetic PNS axons including their varicosities release epinephrine and other mediators locally in diseased adventitia segments to promote the formation of immune cell aggregates and thereby sustain or participate in a robustly remodeled and densely innervated cardiovascular system within the adventitia NICI in late stage atherosclerosis. Therefore, our body of data is consistent with both the CNS and the PNS participating in the control of plaque growth by both local molecular cues and electrical activity projected from the CNS. Future studies should be aimed at the identification of neurons directly targeted by TRPV1[10,11], and other channel transducers[14] in both the PNS and the CNS. Once CNS and PNS neurons will have been defined as direct atherosclerosis targets or effectors, experiments should consider long-term modulation of these neurons to interrogate the impact of each neuron subtype on plaque burden or other yet to be determined impacts. Though the contour of a functional ABC is consistent with our current data, a more advanced and categorically defined atherosclerosis ABC portrait should include the identification of the direct and indirect connectivities of the diseased cardiovascular system across different territories of the PNS and the CNS[30,44-47]. These studies may lead to previously unrecognized

treatment strategies beyond the experimental approaches reported here. They could uncover direct targets using pharmaceutical, surgical and bioelectronic modulation of a thus far putative functional ABC before atherosclerosis becomes life-threatening.

Online content

Any methods, additional references, Nature Research reporting summaries, source data, Extended data, supplementary information, acknowledgements, peer review information; details of author contributions and competing interests; and statements of data and code availability are available at.....

References

1 Libby, P., Ridker, P. M. & Hansson, G. K. Progress and challenges in translating the biology of atherosclerosis. *Nature* **473**, 317-325, doi:10.1038/nature10146 (2011).

2 Mohanta, S. K. *et al.* Artery Tertiary Lymphoid Organs Contribute to Innate and Adaptive Immune Responses in Advanced Mouse Atherosclerosis. *Circulation research* **114**, 1772-1787, doi:10.1161/CIRCRESAHA.114.301137 (2014).

3 Grabner, R. *et al.* Lymphotoxin beta receptor signaling promotes tertiary lymphoid organogenesis in the aorta adventitia of aged ApoE-/- mice. *The Journal of experimental medicine* **206**, 233-248, doi:10.1084/jem.20080752 (2009).

4 Hu, D. *et al.* Artery Tertiary Lymphoid Organs Control Aorta Immunity and Protect against Atherosclerosis via Vascular Smooth Muscle Cell Lymphotoxin beta Receptors. *Immunity* **42**, 1100-1115, doi:10.1016/j.immuni.2015.05.015 (2015).

5 Akhavanpoor, M. *et al.* Adventitial inflammation and its interaction with intimal atherosclerotic lesions. *Frontiers in physiology* **5**, 296, doi:10.3389/fphys.2014.00296 (2014).

6 Yin, C., Mohanta, S. K., Srikakulapu, P., Weber, C. & Habenicht, A. J. Artery Tertiary Lymphoid Organs: Powerhouses of Atherosclerosis Immunity. *Frontiers in immunology* **7**, 387, doi:10.3389/fimmu.2016.00387 (2016).

7 Mukouyama, Y. S., Shin, D., Britsch, S., Taniguchi, M. & Anderson, D. J. Sensory nerves determine the pattern of arterial differentiation and blood vessel branching in the skin. *Cell* **109**, 693-705 (2002).

8 Carmeliet, P. & Tessier-Lavigne, M. Common mechanisms of nerve and blood vessel wiring. *Nature* **436**, 193-200, doi:10.1038/nature03875 (2005).

9 Tam, S. J. & Watts, R. J. Connecting vascular and nervous system development: angiogenesis and the blood-brain barrier. *Annual review of neuroscience* **33**, 379-408, doi:10.1146/annurev-neuro-060909-152829 (2010).

10 Julius, D. & Basbaum, A. I. Molecular mechanisms of nociception. *Nature* **413**, 203-210, doi:10.1038/35093019 (2001).

11 Caterina, M. J. *et al.* The capsaicin receptor: a heat-activated ion channel in the pain pathway. *Nature* **389**, 816-824, doi:10.1038/39807 (1997).

12 Patapoutian, A. & Macpherson, L. Channeling pain. *Nature medicine* **12**, 506-507, doi:10.1038/nm0506-506 (2006).

13 Patapoutian, A., Tate, S. & Woolf, C. J. Transient receptor potential channels: targeting pain at the source. *Nature reviews. Drug discovery* **8**, 55-68, doi:10.1038/nrd2757 (2009).

14 Dubin, A. E. & Patapoutian, A. Nociceptors: the sensors of the pain pathway. *The Journal of clinical investigation* **120**, 3760-3772, doi:10.1172/JCI42843 (2010).

15 Yin, C. *et al.* ApoE attenuates unresolvable inflammation by complex formation with activated C1q. *Nature medicine* **25**, 496-506, doi:10.1038/s41591-018-0336-8 (2019).

16 Pavlov, V. A., Chavan, S. S. & Tracey, K. J. Molecular and Functional Neuroscience in Immunity. *Annual review of immunology* **36**, 783-812, doi:10.1146/annurev-immunol-042617-053158 (2018).

17 Brunet, I. *et al.* Netrin-1 controls sympathetic arterial innervation. *The Journal of clinical investigation* **124**, 3230-3240, doi:10.1172/JCI75181 (2014).

18 Andersson, U. & Tracey, K. J. Reflex principles of immunological homeostasis. *Annual review of immunology* **30**, 313-335, doi:10.1146/annurev-immunol-020711-075015 (2012).

19 Steinman, L. Lessons learned at the intersection of immunology and neuroscience. *The Journal of clinical investigation* **122**, 1146-1148, doi:10.1172/JCI63493 (2012).

20 Dutta, P. *et al.* Myocardial infarction accelerates atherosclerosis. *Nature* **487**, 325-329, doi:10.1038/nature11260 (2012).

21 Rosas-Ballina, M. *et al.* Acetylcholine-synthesizing T cells relay neural signals in a vagus nerve circuit. *Science* **334**, 98-101, doi:10.1126/science.1209985 (2011).

22 Sudhof, T. C. *et al.* Synapsins: mosaics of shared and individual domains in a family of synaptic vesicle phosphoproteins. *Science* **245**, 1474-1480, doi:10.1126/science.2506642 (1989).

23 Sudhof, T. C. Towards an Understanding of Synapse Formation. *Neuron* **100**, 276-293, doi:10.1016/j.neuron.2018.09.040 (2018).

24 Zeng, W. *et al.* Sympathetic neuro-adipose connections mediate leptin-driven lipolysis. *Cell* **163**, 84-94, doi:10.1016/j.cell.2015.08.055 (2015).

25 Cserep, C. *et al.* Microglia monitor and protect neuronal function through specialized somatic purinergic junctions. *Science* **367**, 528-537, doi:10.1126/science.aax6752 (2020).

26 Stjarne, L. Basic mechanisms and local modulation of nerve impulse-induced secretion of neurotransmitters from individual sympathetic nerve varicosities. *Rev Physiol Biochem Pharmacol* **112**, 1-137, doi:10.1007/BFb0027496 (1989).

27 Magnon, C. *et al.* Autonomic nerve development contributes to prostate cancer progression. *Science* **341**, 1236361, doi:10.1126/science.1236361 (2013).

28 Laine, P., Naukkarinen, A., Heikkila, L., Penttila, A. & Kovanen, P. T. Adventitial mast cells connect with sensory nerve fibers in atherosclerotic coronary arteries. *Circulation* **101**, 1665-1669 (2000).

29 Chiu, I. M., von Hehn, C. A. & Woolf, C. J. Neurogenic inflammation and the peripheral nervous system in host defense and immunopathology. *Nature neuroscience* **15**, 1063-1067, doi:10.1038/nn.3144 (2012).

30 Han, W. *et al.* A Neural Circuit for Gut-Induced Reward. *Cell* **175**, 665-678 e623, doi:10.1016/j.cell.2018.08.049 (2018).

31 Carnevale, D. *et al.* A cholinergic-sympathetic pathway primes immunity in hypertension and mediates brain-to-spleen communication. *Nature communications* **7**, 13035, doi:10.1038/ncomms13035 (2016).

32 Carnevale, L. *et al.* Celiac Vagus Nerve Stimulation Recapitulates Angiotensin II-Induced Splenic Noradrenergic Activation, Driving Egress of CD8 Effector Cells. *Cell Rep* **33**, 108494, doi:10.1016/j.celrep.2020.108494 (2020).

33 Gerber, K. J., Squires, K. E. & Hepler, J. R. Roles for Regulator of G Protein Signaling Proteins in Synaptic Signaling and Plasticity. *Mol Pharmacol* **89**, 273-286, doi:10.1124/mol.115.102210 (2016).

34 Wirth, T. *et al.* The sympathetic nervous system modulates CD4(+)Foxp3(+) regulatory T cells via noradrenaline-dependent apoptosis in a murine model of lymphoproliferative disease. *Brain, behavior, and immunity* **38**, 100-110, doi:10.1016/j.bbi.2014.01.007 (2014).

35 Carnevale, D. *et al.* The angiogenic factor PlGF mediates a neuroimmune interaction in the spleen to allow the onset of hypertension. *Immunity* **41**, 737-752, doi:10.1016/j.immuni.2014.11.002 (2014).

36 Kaufmann, H., Norcliffe-Kaufmann, L. & Palma, J. A. Baroreflex Dysfunction. *The New England journal of medicine* **382**, 163-178, doi:10.1056/NEJMra1509723 (2020).

37 McMahon, S. B., La Russa, F. & Bennett, D. L. Crosstalk between the nociceptive and immune systems in host defence and disease. *Nature reviews. Neuroscience* **16**, 389-402, doi:10.1038/nrn3946 (2015).

38 Morrison, S. F. & Nakamura, K. Central Mechanisms for Thermoregulation. *Annu Rev Physiol* **81**, 285-308, doi:10.1146/annurev-physiol-020518-114546 (2019).

39 Tracey, K. J. Reflex control of immunity. *Nature reviews. Immunology* **9**, 418-428, doi:10.1038/nri2566 (2009).

40 Talbot, S., Foster, S. L. & Woolf, C. J. Neuroimmunity: Physiology and Pathology. *Annual review of immunology* **34**, 421-447, doi:10.1146/annurev-immunol-041015-055340 (2016).

41 Chu, C., Artis, D. & Chiu, I. M. Neuro-immune Interactions in the Tissues. *Immunity* **52**, 464-474, doi:10.1016/j.immuni.2020.02.017 (2020).
42 Moos, M. P. *et al.* The lamina adventitia is the major site of immune cell accumulation in standard chow-fed apolipoprotein E-deficient mice. *Arteriosclerosis, thrombosis, and vascular biology* **25**, 2386-2391, doi:10.1161/01.ATV.0000187470.31662.fe (2005).
43 Lotzer, K. *et al.* Mouse aorta smooth muscle cells differentiate into lymphoid tissue organizer-like cells on combined tumor necrosis factor receptor-1/lymphotoxin beta-receptor NF-kappaB signaling. *Arteriosclerosis, thrombosis, and vascular biology* **30**, 395-402, doi:10.1161/ATVBAHA.109.191395 (2010).
44 Kwon, J. T. *et al.* An amygdala circuit that suppresses social engagement. *Nature*, doi:10.1038/s41586-021-03413-6 (2021).
45 Chiang, M. C. *et al.* Parabrachial Complex: A Hub for Pain and Aversion. *The Journal of neuroscience : the official journal of the Society for Neuroscience* **39**, 8225-8230, doi:10.1523/JNEUROSCI.1162-19.2019 (2019).
46 Palmiter, R. D. The Parabrachial Nucleus: CGRP Neurons Function as a General Alarm. *Trends Neurosci* **41**, 280-293, doi:10.1016/j.tins.2018.03.007 (2018).
47 Han, S., Soleiman, M. T., Soden, M. E., Zweifel, L. S. & Palmiter, R. D. Elucidating an Affective Pain Circuit that Creates a Threat Memory. *Cell* **162**, 363-374, doi:10.1016/j.cell.2015.05.057 (2015).

Fig.1. Atherosclerosis-associated NICIs emerge in the adventitia adjacent to plaques. a, $NF200^+$ axons in the adventitia (arrows), adventitia-media border (dashed lines, arrow heads) or plaque (P) in aged $Apoe^{-/-}$ abdominal aorta segments. n = 254 sections from 6 WT, 109 sections from 3 $Apoe^{-/-}$ without plaque, 260 sections from 9 $Apoe^{-/-}$ with plaque, 271 sections from 9 $Apoe^{-/-}$ with ATLO. SMA, smooth muscle actin. **b**, Sympathetic or sensory nerves innervate ATLOs of $Apoe^{-/-}$ mice. TH^+ axons (arrow heads); $CGRP^+$ axons (arrow); $TRPV1^+CGRP^+$ axons (arrow) in ATLOs. n = TH: 5 WT, 6 $Apoe^{-/-}$; CGRP: 7 WT, 8 $Apoe^{-/-}$; TRPV1: 7 WT, 10 $Apoe^{-/-}$. **c**, Norepinephrine levels in abdominal aorta segments without or with plaque. n = 7 WT, 4 $Apoe^{-/-}$ without plaque, 4 $Apoe^{-/-}$ with plaque and ATLO. **d,** Colocalization of growth-associated protein-43 $(GAP43)^+$ growth cones with NFM^+ axons in ATLOs (arrows). n = 3 WT, 3 $Apoe^{-/-}$. **e**, Expression of synapsin $(Syn)^+$ in NFM^+ axon endings in ATLOs (arrows), and quantification of $NFM^+/TH^+/CGRP^+$ axon endings. Syn^+ axon endings at the ATLO-media border (arrow heads; **video 3**). n = 3 WT, 4 ATLOs of $Apoe^{-/-}$. **f,g**, Combined high resolution confocal and STED images of ATLOs. **f**, Syn^+ axon endings juxtaposed to$CD45^+$ leukocytes at ~40 nm resolution in XY forming neuro-leukocyte junctions. **g,** Syn^+ axon endings juxtaposed toSMA^+ SMCs at ~80 nm resolution in XY forming neuro-SMC junctions. Arrows indicate putative junctions; **video 5,6**. n = 4 ATLOs from 3 $Apoe^{-/-}$ mice. DAPI stains DNA in blue. Experimental data are available in source data tables. Data represent means ± s.e.m. n represents biologically independent animals. Generalized estimating equations (**a**); two-way ANOVA with Bonferroni *post-hoc* test (**b,e**); two-sided unpaired Student's t-test (**d**); one-way ANOVA with Bonferroni *post-hoc* test (**c**). **h**, Schematic choreography of adventitia NICI.

Fig.2. Axon neogenesis and restructuring in adventitia NICIs. a, Light-sheet 3D reconstruction, segmentation and tracing of $NF200^+$ nerves and axons and their spatial relationship with ganglia of the intact abdominal aorta (z = 1.2 mm) in 78 weeks aged WT and $Apoe^{-/-}$ mice (n = 2). 3DISCO clearing and light-sheet imaging of the whole mouse abdominal aorta segment including the periaortic ganglia, the CG (arrow) and the SycG (arrow head) reveal restructuring and axon neogenesis adjacent to atherosclerotic plaques (open triangle; **videos 7,8**)**. b,c,** Light-sheet 3D reconstruction coupled with depth-color-coding of the abdominal aorta and periaortic tissues reveals axon neogenesis (asterisk) in $Apoe^{-/-}$ *vs* WT mice. **b,** $NF200^+$ neuronal projections in 600 µm-thick abdominal aortic tissue (4 µm per z-step) are shown in green, and the aorta with connective tissues visualized by autofluorescence imaging in magenta. **c,** Depth color-coding of neuronal projections at different z levels in a ~300 µm-thick abdominal aorta; **videos 9,10**. Arrow heads and double arrow heads indicate nerve fibers and nerves, respectively. **d,** 3D confocal imaging of TDE-cleared whole mount abdominal aorta (z = 40 µm; 2 µm per z-step) and quantification of $NF200^+$ nerve fiber (axon/nerve) diameters in aged WT and $Apoe^{-/-}$ adventitia (n = 3 WT, 3 $Apoe^{-/-}$). **e**, 3D multiphoton imaging showing extensive branching and sprouting of $NF200^+$ axons (asterisk) preferentially in T cell areas in a TDE-cleared whole mount abdominal aorta containing an ATLO (z = 80 µm; 1 µm per z-step; n = 3 $Apoe^{-/-}$); **video 12**. Open triangle, B cell follicle. Sytox or DAPI stain DNA in blue. Experimental data are available in source data tables. Data represent means ± s.e.m. n represents biologically independent animals. Two-way ANOVA with Bonferroni *post-hoc* test (**d**). **f**, Schematic choreography of PNS restructuring.

Fig.3. A structural ABC connects the adventitia with the CNS. a-g, ATLOs connect to the spinal cord and brain nuclei via PNS ganglia. **a,** Representative image of PRV- immunoreactivity (PRV^+) associated with NFM^+ adventitia axons (arrow) within 30 min post-inoculation (p.i.;n = 3). **b-g**, Representative images and quantification of PRV^+ neurons (arrow) in PNS and CNS neuronal tissues after PRV inoculation in the abdominal aorta. **b**, PRV^+ neurons TH^+ CG at d4 (n = 3 at d4-6). **c**, PRV^+CGRP^+ neurons in thoracic DRGs at d4 (n = 6 at d4, 3 at d5, 6 at d6). **d**, PRV^+ChAT^+ neurons in IML of the thoracic spinal cord at d4 (n = 5 at d4, 4 at d5, 9 at d6). **e**, PRV^+ $ChAT^+$ neurons in the RPa at d4 (n = 6 at d4-6). **f**, PRV^+ TH^+ neurons in the PVN at d5 (6 at d4-6). **g**, PRV^+ neurons in the $CGRP^+$ central nucleus of the amygdala (CeA) at d6 (n = 5 at d5-6). . **h-l**, $cFos^+$ neurons (arrows) in the $Apoe^{-/-}$ CNS, and quantification of $cFos^+NeuN^+$ neurons among total $NeuN^+$ neurons in aged WT and $Apoe^{-/-}$ mice. **h**, $cFos^+$ neurons in spinal cord dorsal horn (DH), ventral horn (VH), and IML (n = 3 WT, 4 $Apoe^{-/-}$). **i**, $cFos^+ChAT^+$ neurons in the RPa (n = 3 WT, 3 $Apoe^{-/-}$). **j**, $cFos^+TH^+$ neurons in PVN (n = 3 WT, 3 $Apoe^{-/-}$). **k**, $cFos^+CGRP^+$ neurons in parabrachial nucleus (PBN) (n = 3 WT, 3 $Apoe^{-/-}$). SCP, superior cerebellar peduncle. **l**, $cFos^+$ neurons in $CGRP^+$ CeA (n = 3 WT, 4 $Apoe^{-/-}$). Insets show 3D reconstructed higher magnification images. Details of each experimental data are available in source data tables. Data represent means ± s.e.m. n represents biologically independent animals. Two-sided unpaired Student's t-test (**g,i-l**); one-way ANOVA with Bonferroni *post-hoc* test (**b-f**); two-way ANOVA with Bonferroni *post-hoc* test (**h**). **m,n**, Schematics of structures in putative ABC sensor and effector.

Fig.4. PNS nerve activities; sympathectomy attenuates atherosclerosis progression. a, Representative raw electrical activity recording signal of SSNA in a time window of 10 min and relative quantification. n = young: 4 WT, 8 Apoe$^{-/-}$; adult: 4 WT, 5 Apoe$^{-/-}$; aged: 10 WT, 13 Apoe$^{-/-}$. **b**, Representative raw electrical activity recording signal of CVNA in a time window of 1 min, and relative quantification. n = adult: 8 WT, 10 Apoe$^{-/-}$; aged: 9 WT, 12 Apoe$^{-/-}$. **c**, Norepinephrine levels, and TH^{+} axon density in abdominal aorta; n = 4 control; 4 OHDA. **d-f**, Effect of 6-OHDA denervation on plaque and ATLO. **d**, CD3e^{+} T cells and B220^{+} B cells in ATLOs; n = 5 control, 6 OHDA. **e**, ATLO number/abdominal aorta, ATLO and plaque sizes; n = 5 control, 6 OHDA. **f**, Plaque vulnerability in abdominal aorta; n = 4 control, 4 OHDA. **g**, Norepinephrine levels, and TH^{+} axon density in abdominal aorta. n = 4 sham; 4 CGX. **h,i**, *In vivo* plaque ultrasound imaging before surgery (basal) and at every 2 months up to 8 months post-CGX. **h**, Ultrasound images of plaques (P, yellow line) in the aortic arch at 8 months post-CGX, and quantification of plaque volume **i**, Ultrasound images of plaques in the abdominal aorta at 8 months post-CGX, and quantification of plaque volume; n = 7 sham, 10 CGX at 0-6 months; 5 sham, 9 CGX at 8 months post-CGX. Abbreviations: AR, aortic root; AscA, ascending aorta; DesA, descending aorta; AbdA, abdominal aorta. **j,k**, Effect of CGX denervation on plaque and ATLO. **j,** CD3e^{+} T cells and B220^{+} B cells in ATLOs; n = 5 sham, 9 CGX. **k**, ATLO number/abdominal aorta, ATLO and plaque (P) sizes. **l,** Plaque vulnerability in abdominal aorta; 4 sham, 5 CGX .. Details of each experimental data are available in source data tables. Data represent means ± s.e.m. n represents biologically independent animals. Two-sided unpaired Student's t-test (**c,e,f,g,k,l**); two-way ANOVA with Bonferroni *post-hoc* test (**a,b**); mixed-model ANOVA with Bonferroni *post-hoc* test (**h,i**). **m,n,** Schematics of nerve activity recording and impact of CGX on plaque and ATLO.

Acknowledgements: We thank Wolfgang Wilfert, Ludwig-Maximilians-Universität München for lipid analyses; Vineela Bontha and Prasad Srikakulapu, Cardiovascular Research Center, University of Virginia, Charlottesville for Apoe knockin breeding and aorta sections; Winfried L. Neuhuber, University of Erlangen-Nuernberg for advice; Michael Schemann, Department of Human Biology, Technical University Munich for ChAT antibody; Mingyang Hong and Xinyi Deng, Institute for cardiovascular prevention (IPEK), Ludwig-Maximilians-Universität München for technical assistance; Johan Duchene, Institute for Cardiovascular Prevention, Ludwig-Maximilians-Universität München for progenitor antibodies. We acknowledge Easemedcontrol for illustrations. This work was funded by The Netherlands Organisation for Applied Scientific Research (TNO): Research Program 'Translational Pharmacology' (KIP 10-059) and Early Research Program 'Body-Brain-Interactions' (ERP 020) to RK, the Deutsche Forschungsgemeinschaft (DFG): MO 3054/1-1 to S.K.M.; YI 133/2-1, YI 133/3-5, LMUexcellent 867949-0 to C.Y.; HA 1083/15-4 and HA 1083/15-5 to A.J.R.H.; grant SFB1123-A3, DFG INST 409/209-1 FUGG and by DFG under Germany's Excellence Strategy within the framework of the Munich Cluster for Systems Neurology (EXC 2145 SyNergy - ID 390857198) to J.B.; Germany's Excellence Strategy within the framework of the Munich Cluster for Systems Neurology (EXC 2145 SyNergy - ID 390857198) to M.D.; ERA-CVD (PLAQUEFIGHT) 01KL1808 to A.J.R.H., G.L., Z.M., and T.G.; the Italian Ministry of Health (MoH): Ricerca Corrente to G.L.; the European Research Council (ERC StG 759921 SymPAtHY) to D.C.; DFG SFB 1123/Z1, INST 409/150-1 FUGG and INST409/97-1 FUGG to R.T.A.M.; the European Research Council (ERC CoG 726318 InflamaTENSION) to T.J.G.; an MRC CDA Fellowship (MR/P009824/2) to G.D.; the German Centre for Cardiovascular Research (DZHK MHA VD1.2), DFG SFB 1123/A1 and A10, the European Research Council (ERC AdG 692511), the DFG Cluster of Excellence SyNergy (EXC 2145 SyNergy 390857198) to C.W.; C.W. is a Van de Laar professor of atherosclerosis.

Author contributions:

S.K.M., and A.J.R.H. conceived the project. S.K.M., and A.J.R.H. conceptualized the study; D.C., and G.L. conceptualized nerve recording and CGX denervation experiments. S.K.M., D.C., G.L., and A.J.R.H. designed, performed, analyzed, supervised experiments, and wrote the manuscript with inputs from all authors. C.W. supervised experiments and participated in writing the manuscript. L.P. and S.K.M. designed, performed and analyzed PRV tracing experiments. Y.L., S.L., T.S., L.C., M.P., Z.M., B.F., K.S., C.Z., X.Z., M.B., B.R.S., R.C., D.H., F.P., and L.H. performed and analyzed experiments. M.B. and D.S. participated in data analyses. P.S., R.N., T.J.G., J.P., H.E., J.M., and Z.M. were involved in human samples analysis. B.G.K., and T.C.M. provided PRV virus constructs and contributed to design and supervision of PRV experiments. A.E., S.S., R.K., and J.B. provided materials and supervised experiments. R.T.A.M. and C.Y. performed and supervised experiments. G.D. contributed to design

and interpretation of CNS neuroanatomy experiments. P.S.O. contributed to writing the manuscript. C.Y., T.C.M., R.K., J.B., T.J.G., Z.M., M.D., G.D., and P.S.O. critically revised the manuscript. All authors contributed to data interpretation.

Conflict of interest: The authors S.K.M., A.J.R.H., C.Y., D.C., G.L., L.C., M.P., F.P., R.C. declare competing financial interests. S.K.M., A.J.R.H., and C.Y. are owners of Easemedcontrol R & D GmbH & Co KG Munich, Germany; S.K.M., AJ.R.H., D.C., G.L., L.C., M.P., F.P., R.C. have been named inventors on a pending patent application related to diagnostics and therapeutic interventions into components of the structural ABC to treat atherosclerosis.

Extended Data:

Neuroimmune cardiovascular interfaces control atherosclerosis

Mohanta SK et al.

Extended Data Fig.1. Atherosclerosis-associated axon neogenesis in ATLOs. a, Schematic view of aorta segments. **b**, Axon density in distinct aorta segments with or without plaque in aged WT and Apoe$^{-/-}$ mice; n = thorax: 361 sections in 3 WT, 121 or 209 sections in 3 Apoe$^{-/-}$ without or with plaque; abdomen: 254 sections in 6 WT, 109 sections in 3 Apoe$^{-/-}$ without plaque, 260 sections in 9 Apoe$^{-/-}$ with plaque. **c**, Axon density in thoracic (T) and abdominal (A) aorta segments with or without artery branches in non-atherosclerotic aorta segments; n = 61 or 148 sections without or with branch in 3 WT, 30 or 58 sections without or with branch in 3 Apoe$^{-/-}$ without plaque. **d**, Axon density in WT *vs* Apoe$^{-/-}$ aorta segments with plaque; n = 12-116 sections in 3 WT, 17-71 sections in 3 Apoe$^{-/-}$. Abbreviations: AR, aortic root; AA, aortic arch; ICA, intercostal artery; CA, celiac artery; SMA, superior mesenteric artery; RRA, right renal artery; LRA, left renal artery. **e**, Pearson correlation coefficient of axon density with plaque size in thorax and abdomen. n = 3 Apoe$^{-/-}$ mice. **f**, Enumeration of tubulin-β3 (TUBB3)$^{+}$ immature axons; n = 3 WT, 3 ATLO. **g**, Detection of synaptophysin (Synpt^{+}) axon endings (arrow) in ATLOs, their accumulation (arrow heads) at ATLO-media border (dashed line) and quantification in WT adventitia *vs* ATLOs; n = 4 WT, 4 ATLO; **video 4**. **h,** High resolution 3D reconstruction showing colocalization of CD68^{+} macrophages/monocytes, CD11c^{+} dendritic cells and CD3e^{+} T cells with NF200^{+} axons in ATLOs and their distance from adjacent axons (n = 4 ATLOs per cell-type). **i**, Colocalization of CD3e^{+} T cells with TH^{+} axons in ATLOs (n = 3). Arrows indicate interaction sites that are <1 µm apart; **video 1**. **j,** Synapsin (Syn)$^{+}$ axon endings in WT adventitia and ATLO and accumulation of Syn^{+} puncta at ATLO-media border (arrowheads); **video 3**. n = 3 WT, 3 Apoe$^{-/-}$. **k,l**, Colocalization of Syn^{+} or Synpt^{+} axon endings with CD45^{+} leukocyte forming axon-leukocyte junctions in ATLOs (arrowheads); n = 2; **video 2**. **m**, ATLOs lack ChAT^{+}NFM^{+} parasympathetic axons but harbor ChAT^{+} leukocytes (arrow); quantification of ChAT^{+} T- and B-cells in ATLOs *vs* WT adventitia (n = 3 WT and 3 Apoe$^{-/-}$) (FOV, field of view). **n**, Flow cytometry contour plots and quantification of ChAT^{+} T/B cells in ATLOs, RLNs and spleen (Spl) (n = 3 independent experiments, 2-3 mice per experiment). **o-r**, ADRβ2 expression in ATLOs. **o**, Differential gene expression of *Adrb* subtypes in aged WT *vs* Apoe$^{-/-}$ adventitia or plaque (n = 6 WT, 4 Apoe$^{-/-}$ no plaque, 4 ATLO, 3 plaque). **p**, 3D surface rendering of ADRβ2 expression in CD3e^{+} T cell in ATLO (n = 3). **q**, Flow cytometry gating strategy for immune cells. **r**, Flow cytometry contour plots and quantification of ADRβ2-expressing CD4^{+} T cells, CD4^{+}CD44^{+}CD62L^{-} T_{EM} cells, CD8^{+} T cells and B220^{+} B cells in ATLOs *vs* RLNs and spleen (n = 5 independent experiments, 1-2 mice per experiment). DAPI stains DNA in blue. Data represent means ± s.e.m. n represents biologically independent animals. Generalized estimating equations (**b,c,d**); two-sided unpaired Student´s t-test (**f,g,m**); one-way ANOVA with Bonferroni *post-hoc* test (**h,nr**); Generalized linear model with Bonferroni *post-hoc* test (**o**).

Extended Data Fig.2. Aorta transcriptomes for atherosclerosis-associated axon neogenesis in ATLOs. a-d, Gene expression in WT and Apoe$^{-/-}$ aorta during aging. **a,** Heatmaps of differentially regulated NS development genes (left) and respective NS-related GO terms (right). **b-d**, Quantification of selected candidate genes for axon neogenesis (**b**), axon guidance (**c**), and synaptic transmission (**d**). n = 3 WT, 3 Apoe$^{-/-}$ aorta per group. **e-h**, Gene expression in aged aorta laminae. **e,** Heatmaps show differentially expressed NS-related GO terms in laser capture microdissection-derived aged WT vs Apoe$^{-/-}$ aorta adventitia and plaque. **f-h**, Quantification of candidate genes associated with axon neogenesis (**f**), axon guidance (**g**), and synaptic transmission (**h**). n = 3 WT adventitia, 4 Apoe$^{-/-}$ adventitia no plaque, 4 ATLO, 3 plaque. **i**, Schematic view of laser capture microdissection-derived aged aorta laminae, and numbers of statistically significant (t-test with Benjamini-Hochberg correction) and differentially regulated NS development genes in two-tissue comparisons. n = 3 WT, 4 Apoe$^{-/-}$ no plaque, 4 ATLO, 3 plaque. **j,** Heatmaps show differentially expressed NS-related GO terms in aged WT and Apoe$^{-/-}$ RLN vs ATLO. **k**, Quantification of selected candidate genes. **l,m**, Comparison of selected candidate NS-genes in aged WT vs Apoe$^{-/-}$ RLN (**l**) and spleen (**m**). n = 3 WT RLN or spleen, 3 Apoe$^{-/-}$ RLN or spleen, and 4 ATLOs. Cluster analyses were performed using ANOVA with Benjamini-Hochberg correction (**a,e,j**). Signal intensities and statistics are reported in supplementary Tables1-5. **n,** Detection and enumeration of ALDH1^{+} axons (arrow) in WT adventitia vs ATLO (n 3WT, 5 Apoe$^{-/-}$). **o**, Detection of NGF-expressing periaxonal cells (arrow) and non-neuronal cells (arrowhead), and their quantification in WT adventitita *vs* ATLOs (n= 3 WT, 3 Apoe$^{-/-}$). Data represent means ± s.e.m. n represents biologically independent animals. Generalized linear model with Bonferroni *post-hoc* test (**b-d**,**f-h,k**); two-sided unpaired Student´s t-test (**n,o**); multiple unpaired t-test corrected for multiple comparisons (Bonferroni) (**l,m)**.

Extended Data Fig.3. Axon neogenesis, relation to genotype, age, and cause-effect relationship in adventitia NICIs. a, NF200^{+} axon density in subclavian and renal arteries in aged (78 weeks) WT vs Apoe$^{-/-}$ mice with plaque. n = 3 WT, 3 Apoe$^{-/-}$. **b**, Similar NF200^{+} axon density in renal LNs and in splenic red pulp (RP) or white pulp (WP) of aged WT vs Apoe$^{-/-}$. n = RLN: 3 WT and 3 Apoe$^{-/-}$; spleen: 5 WT and 4 Apoe$^{-/-}$. **c**, Analyses of serum and spleen norepinephrine levels during aging. n = serum: young: 3 WT, 8 Apoe$^{-/-}$; adult: 6 WT, 5 Apoe$^{-/-}$; aged: 7 WT, 7 Apoe$^{-/-}$; spleen: young: 3 WT, 9 Apoe$^{-/-}$; adult: 9 WT, 9 Apoe$^{-/-}$; aged: 8 WT, 12 Apoe$^{-/-}$. **d,** NF200^{+}, TH^{+}, and CGRP^{+} axon density in the aortic root adventitia adjacent to plaques (paraffin sections) in adult (30 weeks) Ldlr$^{-/-}$ on a Western diet (WD) (n =5) vs WT mice (n =4). **e**, NF200^{+}, TH^{+}, and CGRP^{+} axon density in the aortic root adventitia (frozen sections) in adult (32 weeks) Apoe$^{-/-}$ (n =4) *vs* WT mice (n =3) . **f**, Analysis of aortic arch norepinephrine levels in adult mice. n = 3 WT, 4 Apoe$^{-/-}$. **g**, Representative OR/H image of abdominal aorta of aged humanized Apoe4 knockin mice on high-fat diet (HFD); comparison of serum total cholesterol (n = 16 WT, 21 Apoe$^{-/-}$, 8 Apoe4 on chow diet, 10 Apoe4 HFD); and NF200^{+}, TH^{+}, and CGRP^{+} axon densities in the abdominal aorta adventitia of Apoe4 HFD vs Apoe4 mice (n = 3 Apoe4, 4 Apoe4 HFD). **h**, Representative OR/H image of abdominal aorta of aged Apoe$^{-/-}$/Ltbr$^{fl/fl/Tagln\text{-}cre}$ mice, and axon densities in the abdominal adventitia of aged Apoe$^{-/-}$/Ltbr$^{fl/fl/Tagln\text{-}cre}$ compared to their Apoe$^{-/-}$ control or WT adventitia. n = 6 WT, 6 Apoe$^{-/-}$, 4 Apoe$^{-/-}$/Ltbr$^{fl/fl/Tagln\text{-}cre}$. Data represent means ± s.e.m. n represents biologically independent animals. Two-way ANOVA

with Bonferroni *post-hoc* test (**a,b,c,d,e,g**); two-sided unpaired Student´s t-test (**f**); factorial ANOVA with Bonferroni *post-hoc* test (**h**).

Extended Data Fig.4. Restructuring of the PNS in the vicinity of adventitia NICIs. a, Approach on tracing in tissue-cleared intact abdominal aorta of young (12 weeks) WT mice. 3D segmentation and manual tracing of $NF200^+$ nerves/axon bundles along their entire paths (800–1200 µm thickness) shows connectivities of the sympathetic CG (yellow) and SycG (light yellow) with the adventitia. An example of a traced axon bundles (red) contacting the adventitia; approximations of diameters of different sizes of nerves/axon bundle connecting the ganglia are indicated. Arrowheads, beginning and ending of the traced axon bundle from adventitia to CG; arrow, direction of tracing. **b,** Light sheet 3D reconstruction images of $NF200^+$ nerves and axons in the intact abdominal aorta and periaortic tissues (autofluorescence, magenta) of aged WT (n=3) and $Apoe^{-/-}$ (n=2) mice showing $NF200^+$ neuronal structures (green) in the 600 µm-thick abdominal aortic segments (4 µm per z-step; arrow, CG; arrowhead, SycG). **c**, Light sheet 3D reconstruction in the intact abdominal aorta of aged $Apoe^{-/-}$ mice showing varicosities (arrows) in axons adjacent to plaque. Inset, single plan image of the 3D projected whole stack (z = 1.2 mm; arrow, varicosities in axons; arrowhead, nerve) (**c**). Dashed line, media; yellow line, plaque. **d,e,** 3D reconstruction and segmentation views of an abdominal aorta region showing $NF200^+$ nerves and axons and their spatial relationship to the intact abdominal aorta (z = 320 µm; 4 µm per z-step) in aged $Apoe^{-/-}$ mice (n=2). Nerves and axons are evident in the vicinity of the aorta; **video 11**. **f**, 3D reconstruction of TDE-cleared whole mount abdominal aorta (z = 80 µm; 1 µm per z-step; n=3) showing $NF200^+$ nerves and axons in the adventitia. White, second harmonic generation (SHG) from collagen in the adventitia. Arrow, axon; double arrowhead, nerve; asterisk, axon neogenesis in ATLO. **g**, $NF200^+$ axons (arrow, arrowhead) in T cell (T) and B cell (B) areas in ATLO, and their quantification in ATLO and $Apoe^{-/-}$ paraaortic lymph node (pLN). n = 7 ATLOs, 4 pLNs. **h**, Single neurofilament L $(NFL)^+$ immature newly formed axons and double NFL^+/neurofilament H $(NFH)^+$ mature axons in aged WT adventitia vs ATLOs (n = 3 WT, 3 $Apoe^{-/-}$). Data represent means ± s.e.m. n represents biologically independent animals. Two-sided unpaired Student´s t-test (**g**); two-way ANOVA with Bonferroni *post-hoc* test (**h**).

Extended Data Fig.5. NICIs in human cardiovascular tissues. a,b, Representative images and quantification of $NF200^+$ and TH^+ axons in the coronary artery (CA) adventitia of healthy control donors vs atherosclerotic CA of cardiac transplant recipients with coronary artery disease (CAD) (paraffin sections, n = 5 healthy CA from organ donors, 10 CA (NF200) or 6 CA (TH) with plaque). Representative images and quantification of $NF200^+$ and TH^+ axons in non-atherosclerotic CAs *vs* early atherosclerotic CA adventitia from cardiac transplant recipients (frozen sections, n = 6 CA (NF200) or 4 CA (TH) nonCAD without plaque; 7 CA (NF200) or 5 CA (TH) CAD with plaque). **c**, Detection and enumeration of $NF200^+$ and TH^+ nerves in the abdominal aorta adventitia of healthy control donors, non-atherosclerotic and atherosclerotic asymptomatic abdominal aortic aneurysm (AAA) aorta (paraffin sections); n = 4 healthy abdominal aorta, 5 AAA no plaque, 16 AAA with plaque. **d**, Aortic norepinephrine levels in healthy vs and atherosclerotic AAA aorta; n = 5 healthy abdominal aorta, 8 AAA with plaque. **e**,

Detection and quantification of $NF200^+$ and TH^+ axons in AAA with TLOs *vs* without TLOs (frozen sections); n = 5 AAA no TLO, 6 AAA with TLO. **f**, HE-stained nerve-TLCs (N-TLCs) in healthy *vs* atherosclerotic CAs; n = 5 healthy CA from organ donors, 10 CA with plaque. **g,** $CD45^+$ N-TLCs in adventitial nerves in healthy *vs* atherosclerotic AAA aorta; n = 7 healthy control aorta, 13 AAA with plaque. **h**, $CD45^+$ leukocyte infiltration in adventitial nerves in healthy *vs* atherosclerotic AAA aorta. n = 4 healthy control aorta, 10 AAA with plaque. Data represent means ± s.e.m. n represents biologically independent samples. Two-sided unpaired Student´s t-test (**a,b,d,e**); one-way ANOVA with Bonferroni *post-hoc* test (**c**); two-sided Mann-Whitney U-test (**f-h**). Patient details are reported in supplementary Tables 7 and 8.

Extended Data Fig.6. NICIs in PNS ganglia and nerves in atherosclerosis. a, OR/H-staining shows the presence of epineural tertiary lymphoid cluster (TLC) surrounding PvaGs in aged $Apoe^{-/-}$ mice, but not in aged WT mice (dashed line, media) (n = 12 WT, 20 $Apoe^{-/-}$). **b-f**, Cellularity and structures of TLCs. **b,** TH^+ sympathetic PvaG-TLCs harbor $CD45^+$ leukocytes including $CD68^+$ macrophages (arrow), $CD11c^+$ $MHC\text{-}II^+$ dendritic cells (arrow), $CD3e^+$ T cells (open triangle), $B220^+$ B cells (filled triangle), $CD138^+$ plasma cells (arrow). **c,** $Foxp3^+$ T regulatory cells (arrow), $Ki67^+$ proliferating centrocytes in germinal center (PNA^+) (filled triangle), $Ki67^+$ proliferating B cells (arrow), IgM^+ plasma cells (filled triangle). **d,** $PNAd^+$ high endothelial venules (HEV) (arrow), $Coll\text{-}IV^+$ or $Meca32^+$ blood vessels (open arrow, arrow), $Lyve1^+$ lymph vessels (open triangle), $ER\text{-}TR7^+$ conduits (open arrow) or $ER\text{-}TR7^+$ epineurium (filled triangle) and their connection with HEVs (arrow). **e,** Nerve-TLCs contain $CD45^+$ leukocytes including $CD68^+$ macrophages, $CD3e^+$ T cells (open triangle), $B220^+$ B cells (filled triangle), $CD138^+$ plasma cells (arrow), $PNAd^+$ HEVs (arrow), Meca 32^+ blood vessels (arrow), $Lyve1^+$ lymph vessels (open triangle), and $ER\text{-}TR7^+$ conduits (open arrow). **f,** DRG-TLCs around epineuria adjacent to spinal meninges (arrow head) contain $CD68^+$ macrophages (arrow) and $B220^+$ B cells (**f**). n = PvaG: 19 $Apoe^{-/-}$; nerves: 12 $Apoe^{-/-}$; DRGs: 7 $Apoe^{-/-}$. **g**, Morphometry of epineural clusters in PvaG (n = 12 WT, 20 $Apoe^{-/-}$), nerves (n = 8 WT, 12 $Apoe^{-/-}$) and DRGs (n = 5 WT, 7 $Apoe^{-/-}$) in aged mice. Each sphere represents the total number of clusters per mouse. **h**, Pearson correlation coefficient of PvaG-TLC sizes (TLC/PvaG area) with both plaque sizes (intima/media area) and ATLO sizes (adventitia/media area) (n = 15 PvaG-TLCs). One symbol represents the mean value of one individual variable. **i**, TLO stages of epineural clusters in PvaG (n = 19 $Apoe^{-/-}$), nerves (n = 12 $Apoe^{-/-}$) and DRGs (n = 7 $Apoe^{-/-}$). Each sphere represents TLO stages per tissue. **j**, Heatmaps of LCM-derived PvaG microarrays show differentially regulated genes in respective immuno-inflammation-related GO terms in aged WT *vs* $Apoe^{-/-}$ PvaGs. Analyses were performed using two-sided unpaired Student's t test. n = 5 WT PvaGs, 6 $Apoe^{-/-}$ PvaGs. **k**,**l** , Quantitative comparisons of differentially expressed up-regulated genes for *cytokine activity*, *mast cell activation*, *complement activation*, *nervous system development*, and *axonogenesis* in WT *vs* $Apoe^{-/-}$ PvaGs. (n = 5 WT PvaGs, 6 $Apoe^{-/-}$ PvaG). Signal intensities and statistics are reported in supplementary Table 6. **m**, Sympathetic gene expression in LCM-derived PvaG. n = 8 PvaGs. **n**, Detection of CXCL13 expression in WT and $Apoe^{-/-}$ PvaGs in B cell follicles (open triangle) and in PvaG neuronal cell bodies (filled triangle). **o**, Schematic choreographies of PvaG-TLCs, N-TLCs, and DRG-TLCs. **p**, Enumeration of infiltrating

intraganglionic $CD68^+$ macrophages, $CD3e^+$ T cells, and Giemsa-stained mast cells within PvaGs, and thoraco-lumbar DRGs (**i**). n = PvaG: 6 WT, 8 $Apoe^{-/-}$; DRGs: 3 WT, 5 $Apoe^{-/-}$. Data represent means ± s.e.m. n represents biologically independent animals. Two-sided Mann-Whitney U-test (**g,i**); Pearson bivariate correlation (**h**); multiple unpaired t-test corrected for multiple comparisons (Bonferroni) (**k,l**); one way ANOVA with Bonferroni *post-hoc* test (**m**); Two-sided unpaired Student´s t-test (**p**).

Extended Data Fig.7. Distinct pattern of CNS nuclei participates in the formation of the ABC. a, Schematic of PRV injection site in the perirenal abdominal aorta. **b,** Schematic of polysynaptic PRV retrograde migration from ATLO to brain. **c**, *In-situ* detection of India ink around the abdominal aorta and in RLN (left), but not in the kidney (right). Histological detection of ink in the adventitia, paraaortic adipose tissue (arrow) and within RLN (arrowhead), but not in the PvaG soma 2 days post-injection (n = 5 aged WT). **d,** PRV^+ neurons (arrow) in TH^+ sympathetic PvaGs at d2 or SycGs at d4 p.i., and their quantification. **e**, PRV^+ neurons in thoracic 6-13^{th} DRGs of aged $Apoe^{-/-}$ mice at d4; n = 4 per time point. **f**, Mapping of PRV^+ neurons from ATLO to brain until d4. n = 4 for PvaG, 3 for CG; 5 for IML; 6 for RPa; 6 for PVN . Each circle represents mean of PRV^+ neurons, arrow indicates direction of PRV migration, and color indicates the p.i. day. **g,** Quantification PRV^+ neurons in 27 distinct brain nuclei at 4-6d after abdominal aorta inoculation; n = 6 per time point. **h**, Anatomical locations of brain nuclei in **g** according to the Allen Mouse Brain Atlas (sagittal view). **i,** Connectivity mapping of PRV migration over time in 28 different neural tissues (from peripheral ganglia to higher brain nuclei depicted in **f,g**) after abdominal aorta inoculation. **j**, Anatomical representation (sagittal view) of neural tissues in **i** according to the Allen Mouse Brain Connectivity Atlas. Each circle represents mean of PRV^+ neurons, arrow indicates direction of PRV migration, and color indicates the p.i. day.. **k,l**, Quantitative comparisons of PRV^+ neurons in IML of the spinal cord and 27 distinct brain nuclei (**k**), and their anatomical mapping (**l**) at 6d p.i. into the abdominal aorta *vs* control target tissues: right eye, psoas major lumbar muscle, kidney, and blood; n = 4 per group. Data represent means ± s.e.m. n represents biologically independent animals. Mixed-model ANOVA with Bonferroni *post-hoc* test (**d,e**). Abbreviations: gigantocellular reticular nucleus-alpha (GiA), raphe pallidus (RPa), lateral paragigangtocellular nuclei (LPGi), lateral reticular nucleus (LRt); Raphe obscurus nucleus (Rob); rostroventral lateral medulla (RVLM); area postrema (AP); repositus nucleus (Pr); locus coeruleus (LC); Barrington's nucleus (Bar); noradrenaline cell group 5 (A5); laterodorsal tegmental nucleus (LDTg); ventrolateral periaqueductal gray (VLPAG); lateral periaqueductal gray (LPAG); medial lemniscus (ml); peduncular part of lateral hypothalamus (PLH); dorsomedial hypothalamic nucleus (DM); ventromedial hypothalamic nucleus (VMH); arcuate hypothalamic nucleus (Arc); suprachiasmatic nucleus (Sch); cortical amygdala (CoA); lateral amygdala (LA); medial amygdala (MeA); central amygdala (CeA); intergeniculate leaflet of the thalamus (IGL); and piriform cortex (Pir).

Extended Data Fig.8. Specificity of ABC circuit in aged Apoe$^{-/-}$ mice. a,b, ATLOs are innervated by nodose ganglia (NG) neurons or other parasympathetic efferents. **a**, Localization and quantification of PRV^{+} neurons in the NG, 10N and NTS in 3-6d p.i. after abdominal aorta inoculation. Detection of PRV^{+}ChAT^{+} cholinergic neurons in 10N at d6 after abdominal aorta inoculation (right). n = d4: 3 mice; d5: 3 mice (NG,10N); 6 mice (NTS); d6: 4 mice (NG); 6 mice (10N, NTS). Arrow indicates double positive neuron. **b,** Localization and quantification of PRV^{+} neurons in the NG, 10N and NTS in 2-4d p.i. after stomach wall inoculation; n = d2,3: 3 mice; d4: 4 mice. **c,** Quantification of PRV^{+} neurons in medulla, hypothalamic and amygdala nuclei at d6 p.i. in the abdominal aorta; n = 3 WT, 4 Apoe$^{-/-}$. **d**, PRV^{+}TH^{+} neurons among total TH^{+} neurons in sympathetic brain nuclei including RVLM, LC and A5 in aged WT *vs* Apoe$^{-/-}$ mice; n = 3 WT, 3 Apoe$^{-/-}$. **e**, Quantification of cFos^{+}NeuN^{+} neurons in CoA, LA, MeA nuclei of the amygdala); n = 3 WT, 3 Apoe$^{-/-}$. **f,** Detection of cFos^{+}NeuN^{+} and cFos^{+}TH^{+} neurons in RPa (arrow); n = 2 WT, 3 Apoe$^{-/-}$. **g**, Detection of cFos^{+}ChAT^{+} neurons in LPGi (arrow). n = 2 WT, 2 Apoe$^{-/-}$. **h,** Detection and quantification of cFos^{+}NeuN^{+} neurons among total NeuN^{+} neurons in TH^{+} LC (arrow); n = 3 WT, 4 Apoe$^{-/-}$. **i**, Detection of cFos^{+} neurons within CGRP^{+} axon field in the NTS. n = 2 WT, 2 Apoe$^{-/-}$. Data represent means ± s.e.m. n represents biologically independent animals. Mixed-model ANOVA with Bonferroni *post-hoc* test (**a,b**); multiple unpaired t-test corrected for multiple comparisons (Bonferroni) (**c,d,e**); two-sided unpaired Student´s t-test (**h**).

Extended Data Fig.9. Atherosclerosis, cardiac imaging, blood pressure and heart rate variability. a, *In vivo* ultrasound images followed by 3D reconstructions of aorta and plaque volumes *vs* corresponding *in-situ* images in aortic arch and abdominal aorta of WT and Apoe$^{-/-}$ mice (n = young: 4 WT, 8 Apoe$^{-/-}$; adult: 12 WT, 17 Apoe$^{-/-}$; aged: 21 WT, 24 Apoe$^{-/-}$); **video 13**. **b-e**, Imaging of an abdominal plaque using ultrasound-imaging and histology in aged Apoe$^{-/-}$ mice. **b,** B-mode echo images of the abdominal plaque (P) (yellow line). **c,** 3D reconstruction of B-mode echo images (plaque in yellow). **d,** Histological detection of OR/H stained lipid-rich plaque area (red). **e,** Pearson correlation of abdominal aorta plaque volume measured by ultrasound *vs* plaque size (intima/media ratio) measured by histology. n = 9 aged Apoe$^{-/-}$ mice for ultrasound imaging before sacrifice and for histology in the same mice postmortem. Abbreviations: RRA, right renal artery; Abd. aorta, abdominal aorta. **f**, Echocardiographic assessment of cardiac functional and structural parameters in aged WT and Apoe$^{-/-}$ mice (n = 20 WT and 20 Apoe$^{-/-}$). **g**, Analysis of the heart rate variability (HRV) across life span in young and aged Apoe$^{-/-}$ vs WT mice. (n = young: 4 WT, 4 Apoe$^{-/-}$; aged: 3 WT, 4 Apoe$^{-/-}$). **h**, Radiotelemetric analysis of systolic and diastolic blood pressure measurements in young and aged Apoe$^{-/-}$ vs WT mice across lifespan (n = young: 4 WT, 4 Apoe$^{-/-}$; aged: 3 WT, 4 Apoe$^{-/-}$). Blood pressure and HRV were continuously measured for 3 days, during night and day. Average values of nocturnal and diurnal blood pressure for the 3 days of measurements are shown. Measurements of cardiovascular parameters during aging are reported in supplementary Tables 9 and 10. Data represent means ± s.e.m. n represents biologically independent animals. Two-sided unpaired Student´s t-test (**f**); mixed-model ANOVA with Bonferroni *post-hoc* test (**g,h**).

Extended Data Fig.10. The SNS promotes atherosclerosis during aging. a, Spearman correlation coefficients of SSNA vs plaque volume in aortic arch and abdominal aorta in young, adult and aged Apoe$^{-/-}$ mice (n = 26 mice). **b**, Representative raw signals of SSNA in a time window of 10 min and relative quantification of SSNA spikes in adult and aged Apoe$^{-/-}$ mice before and after Celiac vagotomy (CVNX) (n = 6 adult and 7 aged). **c**, Levels of *neuron activation*-related genes in LCM-derived sympathetic PvaGs in aged WT *vs* Apoe$^{-/-}$ mice (n = 5 WT PvaGs, 6 Apoe$^{-/-}$ PVaGs). Signal intensities and statistics are reported in supplementary Table 6. **d**, Approach to 4 weeks 6-OHDA-induced chemical sympathetic denervation in aged Apoe$^{-/-}$ mice. **e**, TH^{+} neurons in the locus coeruleus (n = 5 control and 5 OHDA). **f**, Analysis of spleen norepinephrine (n = 4 control and 7 OHDA), splenic TH^{+} area (n = 4 control and 4 OHDA), and aortic root TH^{+} area (n = 3 control and 3 OHDA). **g,h**, Effect of 6-OHDA denervation on plaque and ATLO. **g,** OR/H stained abdominal aorta showing ATLO cellularity. (**h,** Quantification of abdominal aorta media area; macrophage area (CD68^{+}), necrotic core area, SMC area (SMA^{+}), collagen area (Sirius red^{+}), fibrous cap thickness in plaque; and CD3e^{+}Foxp3^{+} T regulatory cells in ATLO ; n = 4 control and 4 OHDA. **i**, Measurement of serum cholesterol (n = 6 control and 8 OHDA), relative organ weight (n = 5 per group). **j,** Flow cytometry gating strategies and enumeration of Lin^{-}Sca1^{+}Kit^{+}CD150^{+}CD48^{-} hematopoietic stem cells (HSC) gated from LSK (Lin^{-}Sca1^{+}Kit^{+}) or Lin^{-}Sca1^{-}Kit^{+}CD34^{+}CD16/32^{+} granulocyte-macrophage progenitors (GMP) gated from myeloid progenitor cells (MPC) (Lin^{-}Sca1^{+}Kit^{-}) in the bone marrow from total live cells (n = 5 control and 5 OHDA). (**k,** Gating strategies and quantification of CD11c^{+}CD11b^{+} myeloid cells and CD4^{+}Foxp3^{+} T regulatory cells in spleen and RLN from total live cells (n = 5 control and 5 OHDA). **l**, Approach to 8 months CGX selective surgical denervation in adult Apoe$^{-/-}$ mice. **m**, Analysis of spleen norepinephrine (n = 4 sham and 5 CGX), aortic root TH^{+} area (n = 4 sham and 5 CGX), and root plaque size (n = 4 sham and 7 CGX). **n,** Changes in serum cholesterol (n = 3 sham and 9 CGX); relative organ weights after 8 months of surgery (n = 4 sham and 9 CGX). **o**, Flow cytometry gating strategy and quantification of number of CD11b^{+} myeloid cells and CD4^{+}Foxp3^{+} T regulatory cells in spleen and RLN from total live cells (n = 4 sham; 4 CGX). **p,q**, Effect of surgical denervation on ATLO and plaque cellularity. **p,** Histological staining shows ATLO cellularity., **q,** Quantification of abdominal aorta media area; macrophage area (CD68^{+}), necrotic core area, SMC area (SMA^{+}), collagen area (Sirius red^{+}), fibrous cap thickness in plaque; and CD3e^{+}Foxp3^{+} T regulatory cells in ATLO ; n = 4 sham, 5 CGX. **r,** Analyses of internal diameter and ß-stiffness in ascending aorta and abdominal aorta of sham and CGX- mice before surgery (Basal) and 8 months after surgery. **s,** Systolic and diastolic blood pressure measurement (Basal) and at every 2 months up to 8 months after surgery n = **r,s**: 7 sham, 10 CGX before surgery, and 5 sham, 9 CGX at 8 months post-CGX. Data represent means ± s.e.m. n represents biologically independent animals. Two-way ANOVA with Bonferroni *post-hoc* test (**b,j,k,o**); two-sided unpaired Student´s t-test (**e,f,h,i,m,n,q**); multiple unpaired t-test corrected for multiple comparisons (Bonferroni) (**c,i,n**); mixed-model ANOVA with Bonferroni *post-hoc* test (**r,s**). **t**, Comparison of short-term (4 weeks) pharmacological deletion of the SNS and long-term (8 months) outcome of CGX on plaque and ATLO.

Extended Data Fig.11. Schematics of ABC sensor and ABC effector. a, Adventitia NICIs initiate the ABC using sensory neurons of DRGs to enter the CNS via the spinal cord dorsal horn and - from there – projects to the brain stem medulla oblongata. **b**, SNS efferents project from

hypothalamic and brainstem nuclei to the spinal cord and - from there - to the adventitia via the CG, while vagal efferents originating in the medulla oblongata project to the CG - after traversing the NG in the neck - to create an ABC effector.

MATERIALS AND METHODS

Mice

C57BL/6J WT and Apoe$^{-/-}$ mice on the C57BL/6J background (a widely used mouse model of atherosclerosis)[2] were purchased from the Jackson Laboratories and housed in the animal facilities of Munich University, Germany or IRCCS Neuromed, Italy. WT and Apoe$^{-/-}$ mice were maintained on a standard rodent chow diet until 78-80 weeks age. Ldlr$^{-/-}$ mice on C57BL/6J background were bred at the Netherlands Organization for Applied Scientific Research (TNO) at the Division of Metabolic Health Research (Leiden, The Netherlands; substrain is referred to as Ldlr$^{-/-}$ Leiden)[48], and maintained on a standard rodent chow or fed a Western diet (D12451, Research Diets, USA) containing 45% kcal fat from lard, 35% kcal from carbohydrates (primarily sucrose), and 20% kcal protein (casein) for 16 weeks starting at the age of 14 weeks. Apoe4 knock-in (Apoe4) mice on C57BL/6J background were purchased from Taconic, USA[15] and maintained in the animal facilities of Jena or Munich University on a standard rodent chow or fed a high-fat diet (Altromin, Germany containing 15.8% fat, 1.25% cholesterol, and 0.5% sodium cholate for 16 weeks starting at the age of 62 weeks. Apoe$^{-/-}$/Ltbr$^{fl/flTagln\text{-}cre}$ mice on C57BL/6J background were generated as previously described[4] and maintained in the animal facilities of Jena or Munich University on a standard rodent chow until 78-80 weeks age. All mice were housed under specific pathogen free conditions in 12/12 h light/dark cycles, at 21°C and 50% humidity with *ad libitum* food and water. To minimize variability, only male mice were used. All mouse experiments were performed according to European guidelines for Care and Use of Laboratory Animals. Procedures were approved by the Committees on Ethics of Animal Experiments of the IRCCS Neuromed, Pozzilli, Italy (D.Lgs 26/2014, permit number 795/2017-PR and 805/2020-PR); the Government of Bavaria (ROB-55.2-2532.Vet_02-17-57 and 6-14); the Government of Thuringia (22-2684-04-02-051/12); and the TNO animal welfare body (DEC-2944, DEC-Zeist, The Netherlands). Animal procedures were conducted according to guidelines of the local Animal Use and Care Committees, and the National Animal Welfare Laws in compliance with European Community specifications on the use of laboratory animals.

Cardiovascular tissues from patients

Samples of human aortic tissue were obtained from the Munich Vascular Biobank of the Department of Vascular and Endovascular Surgery at Klinikum rechts der Isar (Munich, Germany) or INSERM cardiovascular tissue Biobank (member of European BBMRI-RIC organization) or the Department of Cardiovascular Surgery and Transplantation of the Institute of Cardiology, Krakow, Poland or through the NHS Research Scotland Biorepository, Glasgow, UK. Samples were obtained from patients with abdominal aortic aneurysm (AAA) who underwent conventional surgical open repair of the juxtarenal or infrarenal abdominal aorta from Munich Vascular Biobank. Segments of AAA were obtained during AAA repair surgery at the site of maximal dilatation (35 AAA with plaque

and 5 AAA without plaque). Patient samples were age-matched (age 66.1 on average). The study was performed according to the Guidelines of the World Medical Association Declaration of Helsinki. The local ethics committee of the University Hospital of Munich (Number 17-005, 20-0935 and 20-0935), Technical University Hospital Munich (Number. 2799/10), Jagiellonian University (Number 1072.6120.162.2019), West of Scotland REC 4 (10/S0704/60), and INSERM Paris (number 01-024) approved the study and written informed consent for permission was given by all patients. Human coronary arteries (CAs) were obtained from patients with coronary artery disease (CAD), without CAD (nonCAD) from explanted hearts of transplant recipients (age 55.2 on average) from Glasgow, Krakow and INSERM. CAD/nonCAD classification was based on coronary angiography prior to transplant and macroscopic aspect at dissection to confirm the presence of atherosclerotic plaque (supplementary Table 8). In addition, control healthy human CAs (hCAs) were obtained from explanted hearts of organ donors (age 59 on average) from INSERM. Following surgical excision, tissue samples were cleared of surrounding tissues and immediately snap frozen and embedded in Tissue-Tek (Sakura Finetek) or formalin fixed, paraffin embedded, and stored for further analyses[49-51]. Healthy control abdominal aorta segments (juxtarenal) were obtained from living donors who donated kidneys for transplantation (age 59 on average) from Munich Vascular Biobank. Due to the confidentiality policy for kidney transplantation, no information about the medical history of these donors is known except for age and sex. Control aortas were without any atherosclerotic lesions. Adventitia was present in all aorta samples. Clinical data including major risk factors for atherosclerosis and AAA were recorded at the time of surgery and baseline patient characteristics are summarized in supplementary Table 7.

Histology and immunofluorescence

Mouse aortas were prepared and embedded in Tissue-Tek (Sakura Finetek) as previously described[3,52]. Other tissues including spleen, renal lymph node, small intestine, cervical vagus nerve, aortic root, aortic arches and hearts were collected after isolation of aorta and embedded in Tissue-Tek for further analysis. Murine DRGs from thoraco-lumbar spinal cord segment, spinal cord and brain were collected separately, post-fixed overnight in 4% paraformaldehyde at 4° C, protected with 30% sucrose for 48 hours at 4° C and then embedded in Tissue-Tek. In addition, another cohort of the above samples was prepared as perfusion fixed samples and embedded in Tissue-Tek. All tissue blocks were frozen in chilled isopentane over dry ice and tissue blocks were stored at -80° C until cryosectioning. Serial 10 µm-thick frozen tissue sections or 5 µm paraffin sections were prepared and stained with Oil Red O/hematoxylin (OR/H), hematoxylin-eosin (HE) or Giemsa stain as previously described[15,49-52]. Plaque/media/adventitia/ATLO area, PvaG/TLC area, and granulated mast cells in DRG or PvaG were determined using Axio-Imager microscope equipped with Axiovision release 4.8 software (Carl Zeiss, Germany) or Leica DM6000 with LAS-X (V3.5, Leica

microsystems, Germany). Immunostainings were performed as previously described[3,4,15,60-62], using marker antibodies: anti-mouse/human neurofilament 200 (N4142, Sigma, 1:1000), anti-mouse neurofilament M (N4142, Sigma, 1:500), anti-mouse/human neurofilament L (AB9568, Millipore; ab134460, Abcam, 1:500), anti-mouse/human neurofilament H (CH23015, Neuromics, 1:500), anti-mouse tubulin beta-3 (Tuj1, ab18207, Abcam, 1:500), anti-mouse/human growth-associated protein-43 (AB5220, Chemicon; NB300-143, Novus, 1:500), anti-mouse/human tyrosine hydroxylase (AB152, Millipore; P40101-150, Pel Freez Biology, 1:500), anti-mouse calcitonin gene-related peptide (CGRP, C8198, Sigma; ab36001, Abcam, 1:500), anti-mouse choline acetyltransferase (ChAT, Gift from Prof. Schemann, Munich; AB144P, Millipore, 1:500), anti-mouse transient receptor potential cation channel subfamily V member 1 (TRPV1, ACC-030, Alomone Labs, 1:500), anti-mouse/human synapsin1/2 (106 002, Synaptic System, 1:500), anti-mouse synaptophysin (ab14692, Abcam, 1:20), monoclonal smooth muscle alpha-actin-FITC (F3777, Sigma, 1:300), anti-mouse/human nerve growth factor (NGF; ab6199, Abcam, 1:100), anti-mouse NeuN-A488 (MAB377X, Millipore, 1:300), anti-mouse cFos (ab190289, Abcam, 1:1000), anti-mouse aldehyde dehydrogenase 1 A1 (ab23375, Abcam, 1:500), anti-mouse beta-2 adrenergic receptor (ab182136, Abcam, 1:100), anti-mouse CD45 (BZL 01145; Biozol, 1:100), anti-human CD45 (2B11+PD7/26, Agilent, 1:100), anti-mouse CD68 (FA11; Serotec, 1:100), anti-human CD68 (KP1, Agilent, 1:100), anti-mouse CD11c (N418, Serotec, 1:100), anti-mouse MHCII (M5/114.15.2, eBioscience, 1:300), anti-mouse CD3e (145-2C11, BD, 1:100), anti-mouse B220 (RA3-6B2, BD, 1:200), anti-human CD3 (F7.2.38, Agilent, 1:100), anti-mouse CD138 (AF3190, R&D, 1:100), anti-mouse CD35 (8C12, BD, 1:100), anti-mouse CD4 (RM4-5, BD, 1:100), anti-mouse CD8 (YTS105.18, Serotec, 1:100), PNA-FITC (FL-1071-10, Vector Lab, 1:100), anti-mouse Ki67 (M19, Santa Cruz, 1:300), anti-mouse Foxp3 (ab75763, Abcam, 1:100), anti-mouse IgD (11-26c.2a, BD, 1:100), anti-mouse IgM-FITC (II/41, BD, 1:50), anti-mouse IgG1-FITC (A85-1, BD, 1:50), anti-mouse MECA32 (550563, BD, 1:500), Lyve1 (DP3513P, OriGene, 1:100), anti-mouse PNAd (MECA-79, BD, 1:100), anti-mouse collagen IV (2150-1470, Serotec, 1:500), anti-mouse ERTR7 (T-2109, BMA, 1:100), anti-mouse CXCL13 (AF470, R&D, 1:25), anti-human CD31 (JC70A, Agilent, 1:200), and DAPI for DNA. Anti-mouse ChAT antibody (peptide 3) was in-house produced as described previously. ChAT staining was abolished by preincubation with the ChAT antigen (APREST86792; Sigma) as described to demonstrate specificity[53]. PRV-infected cells were identified using a rabbit monoclonal antiserum against the major capsid protein of PRV (pUL19) as described[54]. Secondary antibodies were used as previously described[4]. For negative controls, stainings were performed without primary antibodies or isotype controls. Stained sections were analyzed using a confocal laser scanning microscope (CLSM) 510 META (Carl Zeiss, Germany) or Leica SP8 3X (Leica microsystems, Germany). Images were acquired with identical microscope settings using sequential channel acquisition to avoid cross-talk between fluorophores. Furthermore, non-spectrally overlapping fluorophores were

applied for colocalization analysis. All images were prepared as TIF files by Fiji (ImageJ, NIH) or Leica LAS-X (V3.5) software and exported into Adobe IIIustrator CS6 for figure arrangements.

Murine and human atherosclerotic plaque analysis

Mouse aortas were prepared and plaque sizes and ATLO sizes were quantified in OR/H-stained serial sections of thoracic and abdominal aorta as previously described. Human AAA and CA sections were stained with Hematoxylin-Eosin and Elastic van Gieson (EvG) in order to assess atherosclerosis[49-51]. In paraffin sections, antisera were first optimized using different dilutions to determine the best staining results with minimal background. Following primary antibody incubation, visualization was performed using the LSAB ChemMate Detection Kit (DAKO) or using secondary antibodies according to the manufacturer's instructions[15]. Stained slides were scanned by a ScanScope microscope (Leica) to obtain digital images or by Leica TCS SP8 3X (Leica Microsystems, Germany) or by DM6 B Thunder Imager 3D Tissue (Leica Microsystems, Germany). Cryosections were stained as described above. All images were prepared as TIF files and quantified by Las-X (V3.5) or Fiji software. The plaque vulnerability index was assessed as described[55] with slight modifications. In brief, intima, media, adventitia, necrotic core area and fibrous cap thickness were analyzed by ORO and H&E-stained sections, while collagen content was measured by Picrosirius Red. For each parameter, 3-5 serial sections near the renal arteries at 100 µm interval per mouse were used.

Lipid measurements

Plasma cholesterol and triglycerides were determined by lipid ultracentrifugation in collaboration with Prof. Teupser Munich as described[4].

High Resolution Confocal Microscopy

For 3D high resolution CLSM microscopy, stained samples were imaged on a CLSM510 META microscope (Carl Zeiss, Germany) or a Leica TCS SP8 3X (Leica Microsystems, Germany) equipped with a 63x oil objective (NA1.4) at a scan zoom factor 3.1. Z-stacks of 10 µm aorta section at 0.2-0.3 µm interval per z-step (z=7-8 µm) were used for evaluation of the colocalization of axons with immune cells. Images from different ATLO sections were acquired under identical microscope settings using sequential acquisition of different channels to avoid interference between fluorophores. 3D reconstructions and spatial interactions analyses were performed using Zen 2009 Light Edition software (Zeiss), Leica Application Suite X (LAS-X) (Leica, V3.5, Germany), Imaris 8.4 (Bitplane, Switzerland) and Fiji software.

Super Resolution STED Microscopy

For direct visualization of cell-cell interactions (axon-immune cell and axon-smooth muscle cell junctions/synapses) in ATLOs at nanoscopic optical resolution, stimulated emission depletion (STED) imaging was performed using a Leica SP8 STED 3X microscope (Leica microsystems, Germany)[56]. Aorta sections (10 µm) with ATLOs were simultaneously stained for synapsin, NFM and CD45 or SMA and mounted with high precision cover slips and Prolong®Diamond antifade mountant. 3D STED imaging was performed using a 93X glycerol objective (NA 1.3). A tunable white light laser source was used to optimally excite the applied fluorophores. Depletion was performed at 592 nm, 660 nm and 775 nm for AlexaFluor488, Cy3 and Cy5, respectively. Images were collected in a sequential scanning mode using hybrid diode detectors to maximize signal collection while reducing background noise and the interference between the channels. A CLSM sequence is applied prior to the STED sequences for recording the DAPI signal[15]. Image reconstructions were performed using LAS X (V 3.5, Leica, Germany) and Imaris 8.4 (Bitplane). Deconvolution was performed with the Huygens Professional (V19.10, Scientific Volume, the Netherlands).

Morphometry:

Morphometry of axon and axon ending density. To determine the innervation pattern of nerve axons in the aorta adventitia throughout the arterial wall, we examined serial aorta section at every 100 µm interval in both the thoracic and the abdominal aorta of aged WT and Apoe$^{-/-}$ mice as described previously[4,15,52]. We used aorta preparations containing the adjacent connective tissue together with the adipose tissue up to 1000 µm stretching radially from the external lamina. The aorta preparation encompassed all major aortic branches in thoracic and abdominal segments. From each mouse, we obtained approximately 2,100 sections (10 µm thick) per aorta and analyzed ~210 aorta sections (every 10th serial aorta sections) for adventitia innervation of NF200^{+} axons in 6-9 aged WT and Apoe$^{-/-}$ mice (~625 sections per genotype). Numbers of NF200^{+} axons of at least 5 µm length in the aorta adventitia were manually counted in 100-120 sections of thoracic and abdominal aorta (reaching the common iliac bifurcation) and/or semi-automatically counted using Fiji in 50-60 aorta sections using 20X objective of LSM510-META (Zeiss, Germany) or of Leica TCS SP8 3X (Leica, Germany). The area of aorta adventitia was measured in a 5X objective of an Axiovision microscope equipped with Axiovision release 4.8 software (Zeiss). Adventitia axon and axon ending densities were determined as the number of axons per mm^2 adventitia area. For quantification of axon density in aorta sections around arterial branches: 5-8 sections per aortic root, 10 sections per aortic arch (every 10th section between innominate and left subclavian artery); 3 consecutive serial sections in 12-14 intercostal artery branches; and 5-8 sections per thoracic or abdominal aorta branches were examined in 3-6 aged WT and Apoe$^{-/-}$ mice. All sections before and after branches were defined as aorta sections without branch. After quantification of adventitia axon density in Apoe$^{-/-}$ mice,

aorta sections in thorax and abdomen were categorized into different groups based on the presence of plaque, aortic locations and branches for statistical analyses.

For quantification of different axons, and axon ending densities in ATLOs or WT abdominal adventitia, 5-6 serial abdominal aorta sections of aged WT, Apoe$^{-/-}$, Apoe4, Apoe4 HFD, Apoe$^{-/-}$/Ltbr$^{fl/fl/Tagln\text{-}cre}$ mice (n=3-9) were selected, multicolor (3-4 color) immunostaining were performed, and then categorized into different groups based on the presence of plaque and ATLO or of arterial branches with or without plaque and ATLO. For quantification of different axons densities in aortic root, 4-5 serial aortic root sections of adult WT, Apoe$^{-/-}$, Ldlr$^{-/-}$, and Ldlr$^{-/-}$ mice on Western diet (WD) (n=3-6) were selected and categorized into different groups based on the presence or absence of plaque. For quantification of axons densities in RLN and spleen, 5-6 images in 3-5 serial sections per mouse in 4-6 aged WT and Apoe$^{-/-}$ mice were used. To quantify the differential distribution of NF200^{+} axons in ATLO or paraaortic lymph nodes (pLN) T- and B cell areas, 4-5 serial abdominal aorta sections with ATLO were examined (n=8 Apoe$^{-/-}$ mice) after 4-color immunofluorescence staining using NF200 for axons, CD3e for T cells, B220 for B cells and DAPI for DNA. 3-4 images per ATLO were acquired and axon density was determined separately in T cell and B cell areas.

Morphometry of tertiary lymphoid clusters (TLCs) and immune cell infiltrates. TLCs are irregularly shaped, non-encapsulated leukocyte aggregates attached to the epineurial capsule of PvaG, nerve and DRG unlike the crescent shaped ATLOs adjacent to the aorta external lamina or the capsulated perivascular lymph nodes. For morphometry of PvaGs and PvaG-TLCs, nerve-TLCs, and DRG-TLCs, 400-500 serial aorta sections (every 10th) and 700-800 serial DRG sections per mouse (every 10th) stained with ORO/H were examined. The presence of PvaGs and nerve determined from the external lamina separating the media from the adventitia in the entire thoracic and abdominal aorta of aged WT and Apoe$^{-/-}$ mice. The numbers of PvaG-TLCs were determined in 12 aged WT and 20 aged Apoe$^{-/-}$ mice; nerve-TLCs in 8 aged WT and 12 aged Apoe$^{-/-}$ mice; and DRG-TLCs 5 aged WT and 7 aged Apoe$^{-/-}$ mice. For correlations between PvaG-TLCs, ATLO and atherosclerosis, 3-5 abdominal aorta sections below the renal arteries with PvaG-TLCs and ATLOs were selected (15 PvaG-TLCs in 10 Apoe$^{-/-}$ mice). PvaG-TLC size was determined as PvaG-TLC area : PvaG area ratio, plaque size was determined as intima area : media area ratio, and adventitia size was determined as adventitia area : media area ratio as described[4,52].

For morphometry of immune cell infiltration in PvaGs and DRGs, tissue sections with PvaGs and DRGs were stained for macrophages (CD68), T cells (CD3e), and mast cells (Giemsa) as described above, and respective immune cell populations were quantified by morphometry. For ganglia macrophage density, CD68 positive macrophage areas in PvaGs (3-6 abdominal aorta sections with PvaGs, 6-8 PvaGs per mouse, 6 WT and 8 Apoe$^{-/-}$ mice) and DRGs (3-4 sections per DRG, 6 thoraco-lumbar DRGs per mouse in 3

WT and 5 Apoe$^{-/-}$ mice) were quantified using Image J (NIH, USA) as previously described[15]. Macrophage density was normalized per stained area percentages in PvaGs and DRGs per mouse. For PvaG and DRG T cell density, parallel sections of the same location were used, and numbers of T cells were quantified per mm² tissue area. For PvaG mast cell density, every 10th aorta sections were stained with Giemsa stain and images of 6-8 abdominal PvaGs per mouse (3-8 serial sections per PvaG) in 5 WT and 5 Apoe$^{-/-}$ mice were used. For DRG mast cell density, 3-5 sections per DRG in 3 thoraco-lumbar DRGs per mouse in 3 WT and Apoe$^{-/-}$ mice were stained with Giemsa, and ganglionic mast cells were quantified in PvaGs and DRGs.

Morphometry of cFos^{+} neurons in spinal cord and brain. 20 µm thick serial cross sections of whole spinal cord or whole mouse brain coronal sections were prepared according to the Allen mouse brain and spinal cord atlas map (http://mouse.brain-map.org/) and the Paxinos Atlas[57]. Every 10th serial spinal cord and brain section stained with ORO/H or HE was examined to define the anatomical locations or stained for cFos expressing activated neurons (NeuN^{+}), and their phenotypes: cholinergic (ChAT), catecholaminergic (TH) and peptidergic somatosensory (CGRP) as described above. Images of the entire surface of the tissue sections were acquired with Thunder 3D Tissue Imager (Leica) and processed with LAS-X (V3.5) or Fiji software. Different brain and spinal cord nuclei were anatomically aligned with the Allen mouse brain and spinal cord atlas map and selected for semi-automated quantification of activated neurons from total NeuN^{+} neurons using Fiji. For quantification of cFos^{+} activated neurons, 3 serial sections per nucleus/area per mouse in 3-4 aged WT and Apoe$^{-/-}$ mice were used.

Laser capture microdissection (LCM) and microarray analyses

LCM and microarray analyses of aorta tissue or spleens or RLNs were performed as previously reported with minor modifications[4,58]. Total aorta or spleen of 3 WT and 3 Apoe$^{-/-}$ mice each at 6, 32, and 78 weeks, and LCM-derived arterial wall compartments or RLN at 78 weeks were extracted[4]. PvaG sections of aged WT and Apoe$^{-/-}$ mice were dissected using the PALM MicroBeam system (Carl Zeiss MicroImaging) after 3 minutes hematoxylin staining to distinguish ganglia with or without TLCs. LCM-derived PvaGs were manually collected from the membrane slide using a Leica Q500 microscope. Trizol buffer was used to lyse tissues. RNA preparation and microarray were done as reported previously[59]. cDNA was synthesized, amplified and purified, and the probe was fragmented (0.5 – 12 µg cRNA), followed by hybridizing for 20 h in hybridization buffer according to Affymetrix protocols as described previously[3,58]. Arrays were scanned immediately after staining and scaled to an array trimmed mean of 200 or 500. All further steps were performed using R and Bioconductor. To correct media effects in LCM experiments (error caused by nearby media tissue) on adventitia or plaque measurements a correction procedure was performed: Up-regulated genes in WT

abdominal adventitia, Apoe$^{-/-}$ adventitia, ATLO or plaque filter lists were eliminated for a two-fold higher media value in a control group of 3 WT media arrays (RME <= 0.666)[59]. After applying filters, the resulting list was subjected to a one-factor analysis of variance (ANOVA) with Benjamini and Hochberg correction for multiple testing between several WT and Apoe$^{-/-}$ groups or a Student's t-test ($P \leq 0.05$) for comparing two WT and/or Apoe$^{-/-}$ groups[59]. The resulting total lists of differentially expressed probe sets or genes ($p \leq 0.05$) were used as the basis for detailed lists of GO terms. Microarray data were deposited in the NCBI´s gene expression omnibus (GEO: accession number GSE94044 for adventitia; GSE93954 for ganglia; GSE40156 for aorta, spleen and RLN).

Flow cytometry

Single cell suspensions from aorta, spleen, renal lymph node and bone marrow were prepared and stained as described before[4,60]. Briefly, aorta were digested separately in 1 ml using digestion enzyme cocktail in a water bath with magnetic rotation at 37°C for 50 min. Blood and spleen were incubated with red blood cell lysis buffer for 7 min at room temperature. Samples were rinsed in FACS buffer and stained for 30 min at 4°C into FACS buffer with Fc-block for extracellular staining and combinations of antibodies to define leukocyte and progenitor populations or with antibodies for 45 min at 4°C in fix and permeabilization buffer (eBioscience) for intracellular staining. After incubation, samples were washed and resuspended in FACS buffer before analysis. The following reagents/antibodies were used for flow cytometry: Fixable Viability Dye-eFluor 660 (eBioscience, 65-0864-14, 1:1000); Fixable Viability Dye-eFluor 780 (eBioscience, 65-0865-14, 1:1000); 7-AAD (BioLegend, 420404, 1:200); CD45-PerCP-Cy5.5 (eBioscience, 45-0451-82, clone: 30-F11, 1:200); CD45-V500 (BD, 19264, clone: 30-F11, 1:200); TCRβ-BV605 (BioLegend, 109241, clone: H57-597, 1:100); B220-eFluor 506 (eBioscience, 69-0452-82, clone: RA3-6B2, 1:200); B220-Pacific Blue (BioLegend, 103227, clone: RA3-6B2, 1:200); B220-PerCP-Cy5.5 (BioLegend, 103236, clone: RA3-6B2, 1:200); CD3-Pacific Blue (BioLegend, 100214, clone: 17A2, 1:200); CD4-PE-Cy7 (eBioscience, 25-0041-82, clone: GK1.5, 1:200); CD4-APC-eFluor780 (eBioscience, 47-0041-82, clone: GK1.5, 1:200); CD4-BV650 (BioLegend, 100469, clone: GK1.5, 1:200); CD8a-eFluor 450 (eBioscience, 48-0081-82, clone: 53-6.7, 1:200); CD8a-AmCyan (BioLegend, 100627, clone: 53-6.7, 1:200); CD11b-BV711 (BioLegend, 101241, clone: M1/70, 1:200); CD11b-APC (eBioscience, 17-0112-82, clone: M1/70, 1:200); CD11b-Pacific Blue (BioLegend, 101224, clone: M1/70, 1:200); CD11c-BUV395 (BD, 744180, clone: N418, 1:200), CD11c-Alexa Fluor 488 (eBioscience, 53-0114-82, clone: N418, 1:200); Foxp3-PE (eBioscience, 12-5773-82, clone: FJK-16s, 1:200); CD44-APC (BioLegend, 103012, clone: IM7, 1:200); CD62L-FITC (eBioscience, 11-0621-82, clone: MEL-14, 1:200); Sca-1-BV605 (BD, 563288, clone: D7,1:200); CD135-APC (BioLegend, 135309, clone: A2F10, 1:200); CD127-APC-Cy7 (BioLegend, 135040,clone: A7R34, 1:200); CD117-PE-Cy7 (eBioscience, 25-1171-82, clone: 2B8, 1:1000); CD34-FITC (eBioscience, 11-0341-82, clone: RAM34, 1:500); CD150-PerCP-Cy5.5 (BioLegend,

115921, clone: TC15-12F12.2, 1:200); CD16/32-PE, BioLegend, 149503, clone: 9E9, 1:500), CD16/32-Unconjugated (eBioscience, 14-0161-82, clone: 9E9, 1:250); CD48-BV510 (BioLegend, 103443, clone: HM48-1, 1:500); Gr1-Pacific Blue (BioLegend, 108430, clone: RB6-8C5, 1:1000); and TER119-Pacific Blue (BioLegend, 116232, clone: TER-119). For each experiment, compensation was developed using single staining controls and compensation beads (Invitrogen, 01-2222-41). For all cell types, initial forward scatter versus side-scatter gates were adjusted using splenocytes to include all cells and exclude debris, dead cells were excluded using Fixable Viability Dye (eBioscience) or 7-AAD (BioLegend) before gating for leukocyte and progenitor populations. Cell populations were gated on live cells and defined as T cell: $CD45^+TCR\beta^+$; B cell: $CD45^+B220^+$; $CD4^+$ T cell: $CD45^+TCR\beta^+CD4^+$; $CD8^+$ T cell: $CD45^+TCR\beta^+CD8^+$; effector memory T cells (T_{EM}). $CD4^+CD44^+CD62L^-$; $CD4^+$ Treg: $CD4^+Foxp3^+$; $CD11b^+$ $CD11c^+$ myeloid cell: $CD45^+TCR\beta^-B220^-CD11b^+CD11c^+$; $CD11b^+$ myeloid cell: $CD45^+TCR\beta^-CD11b^+$; bone marrow HSC: $Lin^-Kit^+Sca\text{-}1^+CD150^+CD48^-$; and bone marrow GMP: $Lin^-Kit^-Sca\text{-}1^+CD34^+CD16/32^+$ (lineage comprised CD3, Gr1, CD11b, B220 and TER-119). Data were expressed as percentage of specific cell populations or calculated as cell numbers from 10^6 total live cells. Data were acquired with a FACS Canto II or FACS Celesta or LSRFortessa (BD Biosciences, USA) and analyzed with FlowJo (V10.6, BD)[3,4,60,35].

Tissue clearing:

Whole-body immunostaining, 3DISCO clearing, Light-sheet imaging and tracing. Mice were sacrificed and perfused as previously described[61,62]. After removal of skin and internal organs (intestine, liver, and spleen), mice were post-fixed in 4% PFA for 1d at 4° C and later washed with 0.1 M PBS for 10 min 3 times at RT. The whole body was divided into halves above the diaphragm, and the lower body part containing aorta, aortic branches, perivascular adipose tissue, lymph nodes and ganglia was used for whole-mount staining procedure immediately or stored in PBS containing 0.05% sodium azide (Sigma-Aldrich, 71290) at 4° C for up to 4 wks. After PFA fixation and washing with PBS, all other steps were performed. The decolorization solution was made with 25 volume % dilution of CUBIC reagent for 48 h followed by 3 times 1.5 h PBS washes. Samples were then permeabilized overnight with PBS-gelatin-Triton X-serum (PGTS) solution containing 0.1 M PBS with 0.2% porcine skin gelatin (Sigma, G2500), 0.5% Triton X-100, and 5% goat serum on a shaker as described before followed by incubation with primary antibody (NF200, 1:2000) in PGTS for 10-12 days. Then, samples were washed for 1.5h with PBS 3 times at RT and incubated with secondary antibodies, diluted in PGTS with shaking on an oscillator for 7 days. The secondary antibody was refreshed once after 2 days. Finally, samples were washed for 1.5h three times with PBS and stored at 4°C until clearing.

For shrinkage-mediated imaging of the entire abdominal aorta, we used the organic solvent based 3DISCO clearing protocol with slight modifications[61,62]. The clearing consisted of serial incubations of stained samples in 40 ml of 50%, 70%, 90%, 100%, and 100% tetra-hydro-furanose for 12h each to dehydrate the tissue, then immersion in di-chloro-methanol for 3h at RT to remove lipids. Eventually, samples were incubated in 1/3 benzyl-alcohol + 2/3 benzyl-benzoate for 2-6h until they became transparent.

Single-plane illuminated (light-sheet) image stacks were acquired using an Ultramicroscope II (LaVision BioTec, Germany), ventral to dorsal using a z-step size of 4 µm as described before[61]. Whole-mouse abdominal regions of aged WT and Apoe$^{-/-}$ mice were imaged with a 2X objectives (Olympus MVPLAPO2XC/0.5 NA; working distance = 6 mm) or a 4x objective (Olympus XLFLUOR 4x corrected/0.28 NA; working distance = 10 mm). Tile scans covering the entire specimens were acquired with 20% overlap, and the light-sheet width was adjusted to obtain uniform illumination across the view field. Stitching of tile scans was done via Fiji's stitching plugin as previously described[61,62]. Stitched images were saved in TIFF format and optionally the pre-processed data was compressed in lossless LZW format to reduce storage size and to enable fast processing. We used Imaris 8.4 (Bitplane), Amira (Thermo Fisher), and Fiji for 3D and 2D image visualizations. Image processing, 3D rendering, and video generation were executed by an image processing workstation. For segmentation and manual tracing of different anatomical structures, Amira software (Thermo Fisher) was used. For segmentation of neuronal bundles and ganglia of the celiac plexus, manual tracing was performed using the NF200^{+} signals in the far-red channel (680 nm). All other structures were traced based on the 488 nm autofluorescence using manual tracing with Amira software (Thermo Fisher). NF200^{+} nerves, axon/axon bundles in the aorta adventitia were traced in a dorsoventral manner from the aorta to the contact point with the celiac ganglion or with the chain ganglia in every z-plane along their entire paths between the aorta and adjacent ganglia or along the orthogonal optical slices of the z-stack in xy orientation. To ensure high fidelity tracing of small fibers, the NF200+ signals were manually selected pixel by pixel in every z-plane along the entire path of the nerve fiber between aorta and ganglia. Tracing of an intact nerve fiber along its length across 25-30 consecutive z-slices/planes at every 4 µm interval (100-120 µm thickness) in WT and Apoe$^{-/-}$ mice. For depth-color coding, raw images were deconvoluted with Huygens Professional (V.19.10, Scientific Volume Imaging, the Netherlands) and maximum intensity projections of deconvoluted data were generated with the Leica Application Suite X or with temporal-color code in Fiji. To increase the quality of the images and to enhance the contrast over the background of the axonal endings, we used 'Enhance Local Contrast (CLAHE)' functions in Fiji[60-62].

Whole-mount immunostaining, TDE clearing and imaging. After euthanasia and intracardiac perfusion, *en-face* abdominal aortas were prepared and post-fixed in 4 % paraformaldehyde overnight at 4° C, thoroughly washed in PBS for 10 minutes three

times, blocked and permeabilized for 2 h at RT with 1% BSA, 10% donkey serum, Fc-block and 0.5% Triton X-100. Whole-mount immunostainings were performed by incubating with primary and secondary antibodies in the blocking solution for 24h and 3h, respectively. Primary antibodies included NF200, B220 and CD3e. Sytox (S11380, ThermoFisher) was used to stain DNA. TDE clearing was performed with increasing concentrations of TDE (20 % TDE for 1 h at 37°C, and 47 % TDE 36 h at room temperature) on a rotating shaker as described[60,61,63] by matching refractive indexes of different tissue layers to the solvent and to make the aorta transparent. TDE-cleared whole aorta was imaged from the abluminal side using confocal microscopy (SP8 3X Leica) equipped with 20x objective (NA: 0.75) up to 50 µm of depth. For complete aorta scanning including entire ATLOs and plaques with adjacent adipose tissue (1 mm thickness), we used multi-photon laser scanning microscopy on a Leica SP5II MP as described before[60]. Serial z-scans and tile scans covering the entire aorta tissue were acquired. Raw pictures were deconvoluted with Huygens Professional (V.19.10, Scientific Volume Imaging, the Netherlands) and maximum intensity projections of deconvoluted data were generated with LAS-X (V3.5, Leica). 3D image reconstructions were processed using Imaris 8.4 (Bitplane) and extension of MATLAB R2016b (MathWorks, USA)[60-63] for volumetric analysis of NF200+ axons or axon bundle per voxel of adventitia or ATLOs.

Retrograde PRV tracing

Pseudorabies virus (PRV) is a neuroinvasive alpha herpes virus which is closely related to human herpes simplex virus. It infects neurons and crosses synaptic junctions. PRV strain Bartha (PRV-Ba) is an attenuated live vaccine strain, which can spread transneuronally exclusively in the retrograde direction. It is widely used as a multisynaptically migrating neuronal tracer[64-66].

Mice were deeply anesthetized with sodium pentobarbital (80 mg/kg, i.p.) and the PRV suspension was injected into the caudal tail vein (5 µl, $4.5x10^4$ plaque-forming unit (pfu)/mouse) to rule out PRV infection via the blood circulation[64,65], or into the vitreous body of the right eye (10 µl, $9×10^4$ pfu/mouse) to examine the visual circuit[64]. For PRV injections into kidney, muscle, aorta and stomach, a longitudinal ventral midline laparotomy allowed exposure of abdominal aorta, left kidney, the lumbar psoas muscle, and the stomach after mobilizing the spleen, and the intestine. Care was taken to not remove or disrupt connective tissue or fascial sheaths associated with the injection target prior to injection. 5 µl PRV suspension ($9×10^6$ pfu/ml) was injected into 5 sites of the renal cortex of the left kidney[66] or the lumbar psoas muscle between left renal lymph node and left kidney, or the abdominal aorta adventitia between the superior mesenteric artery and left renal artery, or the greater curvature of the stomach using micro-surgical instruments under an operating microscope (25x magnification). For aorta injection, 1 µl PRV suspension per site was delivered at 15 degrees angle between needle and

abdominal aorta for strictly avoiding penetrating the aorta wall. The virus was pressure-injected over 1 min and the needle was kept in place for 2 min in order to minimize leakage of the virus. After each injection, the site of injection was covered with sterile cotton swabs to further prevent leakage of the virus into the surrounding tissue. After careful irrigation of the entire abdominal cavity with 0.9% sterile and pre-warmed saline, the abdominal surgery procedure was ended by closing the abdominal muscles and skin using 5-0 vicryl sutures (Ethicon) and nylon (Ethicon). Buprenorphine (s.c., 0.05 mg/kg) was injected immediately after surgery for postoperative pain management. Mice were placed into incubators until they had recovered consciousness and returned to their home cage. After injection, each infected mouse was housed in individual cages with ad libitum food and water, and carefully monitored throughout the course of the study.

Mice were sacrificed at 2-6 days p.i., perfusion fixed, ipsilateral- and contralateral eyes, kidney, muscle, stomach, peripheral ganglia, spinal cord and brain were isolated, cryopreserved, and transverse serial cryosections were prepared at 30 µm for eye, 40 µm for spinal cord, 35 µm for brain, and 20 µm for aorta and other tissues. Everything that contacted the PRV-infected mice during the tracing experiments including the micro-syringes, gauzes, cotton balls, cages, food, water were treated as described previously[64-66]. For disposal, all materials were put in a biohazard bag and incinerated according to institutional regulations.

Quantification of PRV-infected neurons: 3-5 consecutive sections per tissue per mouse at 175 µm intervals in at least 3 mice were selected for quantification of PRV immunoreactivity^{+} PRV-IR neurons. Brain and spinal cord nuclei were identified according to the Allen mouse brain and spinal cord atlas map[13] and Allen mouse brain connectivity atlas using whole brain or spinal cord images by Thunder 3D Tissue Imager (Leica). For brain and spinal cord both left and right hemispheres were combined to calculate the average number of PRV-IR^{+} neurons.

Norepinephrine (NE) high sensitivity ELISA

For measurements of norepinephrine level in aorta, aortic arch, spleen and serum in mouse or abdominal aorta of organ donors and aneurysmatic human samples, a Noradrenaline Research ELISA (BA E-5200, Labor Diagnostika Nord) was used. Serum samples were prepared and immediately snap-frozen in liquid nitrogen. Spleen (1/4th), aortic arch, lower abdominal aorta of mouse or human abdominal aorta segments were dissected, immediately snap-frozen in liquid nitrogen and homogenized in a catecholamine-stabilizing solution containing hydrochloric acid (0.01 M), EDTA (1 mM) and sodium metabisulphite (4 mM) at pH 7.5[20]. Homogenized samples were centrifuged at 5000 rpm for 5 min at RT. The supernatants were collected, and the protein concentration measured using NanoDrop (Protein 280, ThermoFisher). Norepinephrine concentration was quantified in duplicate according to the manufacturer's instructions. All tissue samples were normalized to total tissue protein concentration.

Blood pressure measurements

Noninvasive arterial blood pressure measurements were performed by tail-cuff plethysmography (BP-2000 Series II, Visitech Systems) in conscious mice daily, between 10 a.m. and 12 p.m., as previously described[35,67]. Operators were blinded to the experimental group during blood pressure monitoring.

Radiotelemetric blood pressure measurements

Radiotelemetry was used for continuous monitoring of blood pressure and heart rate in freely moving conscious mice as previously described[35,67] (supplementary Table.10). Young (12 weeks) and aged (52 weeks) Apoe$^{-/-}$ and WT littermates were anaesthetized with 5% isoflurane for induction and maintained at 1.5% supplemented with 1 L/min and underwent surgery for HD-X11 implant (DSI). After exposing the left carotid artery with a longitudinal incision, the catheter tip was inserted in the carotid artery and slid to the aortic arch. Intrasurgical monitoring was performed by US aortic arch imaging, performed on the Vevo2100 (Visualsonics, Fujifilm) using the 40 MHz probe to achieve optimal positioning and ensuring radiotelemetric readings quality as described[68]. Radio signals were acquired by Physiotel RPC-1 plates (DSI), sampled and elaborated by Ponemah 6 acquisition and analysis system (DSI). Blood pressure measurements were carried on in a dedicated room with light/dark cycle.

Blood pressure analyses were performed in Ponemah 6. Systolic/diastolic blood pressure, heart rate, interbeat interval were measured in milliseconds, and averaged over blood pressure cycles cleaned from artefacts, and logged every five seconds. Blood pressure measurements were further averaged over the night/day hours to visually inspect the circadian rhythm of the mice.

Heart rate variability analyses were performed in Ponemah 6. The interbeat interval signal was transformed into the frequency domain by FFT on 20 seconds segments, with two overlapping subseries and Hanning windowing. The spectrum was analyzed between 0 and 5 Hz, binning the spectral components in three distinct categories: Very Low Frequency (VLF, 0.01Hz-0.40Hz), Low Frequency (LF,0.40Hz-1.50Hz), High Frequency (HF, 1.50Hz-4.00Hz). Spectral components were normalized in each segment and the ratio between normalized LF/HF was averaged over night/day hours to visually inspect the HRV.

Ultrasonographic analyses

Ultrasonographic analyses were performed with Vevo2100 (Visualsonics, Fujifilm) equipped with 40 and 50 MHz transducers. Mice were anesthetized with isoflurane (5% induction and 1.0%–1.5% maintenance supplemented with 1 L/ min oxygen). Cardiac function was obtained by standard echocardiography[69]. For aortic arch visualization, the 40 MHz ultrasound transducer was placed on the right side of the upper anterior

mediastinum. To standardize this projection, 3 reference points were used: The aortic valve, the pulmonary artery, and the brachiocephalic trunk. To obtain a volumetric quantification of atherosclerotic plaques inside the aortic arch, 3D ultrasound imaging was used, starting from aortic arch projection described above. For the abdominal aorta visualization, the 50 MHz ultrasound transducer was placed on the abdomen area and a longitudinal view of the aorta was obtained. To cover the distance from the diaphragm to the iliac artery bifurcation, two consecutive 3D ultrasound acquisitions were made: the first from diaphragm to the superior mesenteric artery, the second from the superior mesenteric artery to the iliac bifurcation. All 3D images were performed using the following setup: scan distance 5.016mm and step size 0.032 mm, the electrocardiographic (ECG) trigger was set on the P wave and respiration movement artefacts were minimized applying respiration gating. All acquired images were processed with VevoLAB and analyzed by two different operators. Plaque contours were manually drawn whereby the software automatically interpolate the contours and reconstructed the 3D volume. In case of more than one plaque for each aortic tract analyzed, the sum of the plaques volume was reported. Vascular functional analysis was performed as previously described (supplementary Table 9)[70].

Electrophysiological Recordings – Surgery

Mice were subjected to SSNA and CVNA recordings at the age specified in the figure legend and main text. SSNA recordings were performed as previously described[31]. In brief, mice were anaesthetized with 5% isoflurane and maintained with 1.5–2% (supplemented with 1 L/min oxygen). Arterial BP monitoring was performed during the whole recording with a single-tip pressure catheter (Millar, SPR-100) inserted in the left femoral artery and wired to a pressure transducer interface (Millar, MPVS ULTRA). The splenic district was accessed after an abdominal incision by gently moving the intestine of the mouse and the connection between celiac ganglion and spleen was exposed. Then the splenic nerve was isolated from the artery and electrodes were placed beneath it. The bipolar stainless-steel electrodes (MLA1214 Spring Clip Electrodes, ADInstruments) were refined to adapt to the splenic nerve size and to grant a better contact between leads and nerve. The electrodes were wired to a digital amplifier and sampler (Animal Bio Amp, ADInstruments), in which the analog signal was amplified (gain x 10,000) and sampled at 4kHz. Sampled signal was then collected and processed together with arterial pressure signal by a Power Lab acquisition system (ADInstruments). After stabilization of the preparation and adequate signal of nerve activity, the electrodes were further isolated by silicone gel. Nerve activity was recorded for one hour, while continuously monitoring blood pressure. All the data were collected and monitored by LabChart 7 (ADInstruments) running on an online computer. Isoflurane overdose was induced to record 30 minutes of postmortem activity, to estimate systematic and baseline noise[31]. CVNA recordings were performed with the

same experimental procedure, exposing the celiac branch of the vagus nerve and placing the electrodes beneath it, as previously described[32].

Celiac vagotomy was performed while recording SSNA, as previously described[31]. In brief, the celiac branch of the vagus nerve was exposed, before positioning the recording electrodes on the splenic nerve. A silk suture thread was knotted to the distal end of the nerve. After recording two-time windows of SSNA, the nerve was excised pulling the thread, without further manipulations of the splenic area, in order to ensure an optimal stability of the signal, recorded for additional two time windows. The effect was expressed as percentage of SSNA reduction after nerve excision.

Electrophysiological Recordings – Data Analysis

Splenic nerve activity data was collected and analyzed with Lab Chart 7 (Spike Analysis Module). Preprocessing of the signal consisted in digital filtering out electrical cord current with a 50 Hz notch filter and selecting the frequencies of interest by a 300-1,000 Hz band-pass filter, expressing the final signal in μV. Splenic nerve spikes were identified as spikes with intensity above the background noise threshold measured in post-mortem acquisition. Spike counting was performed in two consecutive 10-minute window starting from the electrodes' silicone isolation. Spike count was defined as the total number of spikes counted in a time window, and was obtained by averaging the total counts of two consecutive time windows (of 10-minute each)[31]. The celiac vagus nerve activity data was collected and analyzed with Lab Chart 7 (Spike Analysis Module) and MATLAB (Mathworks), as previously described[32]. The vagus nerve raw signal was amplified and sampled with the same setting of splenic nerve, but digitally filtered by a narrower 300-550 Hz band-pass filter, to avoid high-frequency activity and noise. Then, the signal has been integrated with a time-constant decay of 0.1 seconds to sum up the single spikes contribution to each burst. The integrated signal was exported into MATLAB and then processed with an in-house script to perform a peak analysis. CVNA activity was quantified as number of activation bursts performed in two consecutive 10-minute window starting from the electrodes' silicone isolation. Burst count was defined as the total number of counted peaks of the integrated signal, and was obtained as the average of bursts' count of two consecutive time windows.

Denervation

6-OHDA denervation: Chemical sympathetic ablation was performed by injecting 6-hydroxydopamine (6-OHDA, Sigma)[20]. 6-OHDA was injected i.p. at a dose of 100 mg per kg body weight on day 0 and 250 mg per kg body weight on day 2 (after 48 hours) followed by 250 mg per kg body weight per week until 4 wks. Control group received the same amount of vehicle injection (i.p.) at the same time points. Animals were sacrificed one week after last injection.

Celiac ganglionectomy (CGX): Mice were anaesthetized with 5% isoflurane and subsequently maintained with 1.5-2 % (supplemented with 1 L/min oxygen). CGX was performed as previously described[35,31,71]. Body temperature was maintained between 37°C and 38°C by a homeothermic blanket during the entire surgery. A midline laparotomy was applied, and aorta and celiac artery were exposed. At its rostral pole, the left celiac ganglion receives 2-3 nerve bundles from the left suprarenal ganglion and several smaller bundles from the celiac arterial plexus. Once identified, it was gently removed, taking care to not damage surrounding vessels and tissues. At the end of the surgical procedure, tissues were carefully repositioned into the abdominal cavity. The incision was sutured with reabsorbable thread. For the sham procedure, the ganglion area was exposed, and aorta and celiac artery were exposed, without removing the ganglion. The post-operative course was conducted in housing cages placed in apposite incubators maintained at a temperature of 25°C to facilitate animal recovery. CGX allowed removal of splanchnic innervation, including the splenic nerve and fibers, nerve and fibers innervating the abdominal aorta, and part of celiac vagus nerve. For the sham procedure, mice underwent the same surgery for exposure of the celiac ganglion but without its removal. Atherosclerosis progression was assessed by serial echography (Vevo2100) before the denervation and every 2 months until 8 months post-surgery.

After sacrifice, blood, spleen, and lymph nodes were analyzed to determine the immunological profile by flow cytometry (BD FACS Canto and FACS Celesta V8). To minimize variability, only male mice were used, and animals were randomized to treatments. Phenotype assessment and all the subsequent analyses were performed by researchers blinded to the treatment.

Statistical Analyses

Data were analyzed using the Prism 8 (GraphPad Inc.) and SPSS v.28 (IBM Corp). The ROUT outlier function was used to exclude statistical outliers (Q = 1%). Data distribution and homogeneity of variance were tested by the Shapiro-Wilk and Levene's tests, respectively. For data following normal distribution, two-sided unpaired Student's t-test with Welch correction when appropriate (two groups comparisons) or one-way ANOVA with Bonferroni's post-hoc test (three or more groups). The relationship between two quantitative variables was estimated with Pearson's correlation coefficients. In analyses involving two or more factors, factorial (two- and three-way) ANOVA, generalized linear models (GLM), or mixed model (REML) with Bonferroni's post-hoc test for pairwise comparisons were applied. Spatially paired observations were compared using a 2-sample paired Student's t-test. To compare morphometry data of multiple mouse groups, the generalized estimating equation (GEE) model with Bonferroni post-hoc test to estimate the parameters of a generalized linear model when the data set consists of repeated measures per mouse[3]. Since data sets consist of repeated measures per mouse, the GEE model takes the correlation of these measurements per individual

mouse into account and provides robust estimates for the standard errors of the regression coefficients, i.e. that even under misspecification of the chosen correlation structure, inferences regarding the group differences are still unbiased, which is advantageous when compared to traditional linear regression models[72]. For data violating assumption of normal distribution, Mann-Whitney *U*-test was used for comparison between two groups and Spearman correlation coefficient for bivariate correlations. All experiments were replicated at least three times independently. All tests were two-sided except where indicated. Differences were considered significant for a P-value <0.05. Data were reported as means and standard error of means (s.e.m.) unless otherwise stated.

Reporting summary

Further information on research design is available in the Nature Research Reporting Summary linked to this paper.

Data availability

Microarray data were deposited in the NCBI´s Gene Expression Omnibus repository (GEO: accession number GSE94044 for adventitia; GSE93954 for ganglia; GSE40156 for aorta, spleen and RLN). All other relevant data are available from the corresponding authors upon reasonable request. Source data are provided with this paper.

Methods References

48 Tengeler, A. C. *et al.* Propionic acid and not caproic acid, attenuates nonalcoholic steatohepatitis and improves (cerebro) vascular functions in obese Ldlr−/−. Leiden mice. *The FASEB Journal* **34**, 9575-9593 (2020).

49 Terzian, Z. *et al.* Peristrut microhemorrhages: a possible cause of in-stent neoatherosclerosis? *Cardiovascular Pathology* **26**, 30-38 (2017).

50 Reeps, C. *et al.* Inflammatory infiltrates and neovessels are relevant sources of MMPs in abdominal aortic aneurysm wall. *Pathobiology* **76**, 243-252 (2009).

51 Guzik, T. J. *et al.* Systemic regulation of vascular NAD (P) H oxidase activity and nox isoform expression in human arteries and veins. *Arteriosclerosis, thrombosis, and vascular biology* **24**, 1614-1620 (2004).

52 Mohanta, S., Yin, C., Weber, C., Hu, D. & Habenicht, A. J. Aorta Atherosclerosis Lesion Analysis in Hyperlipidemic Mice. *Bio-protocol* **6** (2016).

53 Schemann, M., Sann, H., Schaaf, C. & Mader, M. Identification of cholinergic neurons in enteric nervous system by antibodies against choline acetyltransferase. *American Journal of Physiology-Gastrointestinal and Liver Physiology* **265**, G1005-G1009 (1993).

54 Klupp, B. G., Granzow, H. & Mettenleiter, T. C. Primary envelopment of pseudorabies virus at the nuclear membrane requires the UL34 gene product. *Journal of Virology* **74**, 10063-10073 (2000).

55 Silvestre-Roig, C. *et al.* Externalized histone H4 orchestrates chronic inflammation by inducing lytic cell death. *Nature* **569**, 236-240, doi:10.1038/s41586-019-1167-6 (2019).

56 Westphal, V. *et al.* Video-rate far-field optical nanoscopy dissects synaptic vesicle movement. *Science* **320**, 246-249, doi:10.1126/science.1154228 (2008).

57 Paxinos, G. & Franklin, K. B. The mouse brain in stereotaxic coordinates. *Elsevier Academic Press* (2007).

58 Yin, C. *et al.* Generation of aorta transcript atlases of wild-type and apolipoprotein E-/- mice by laser capture microdissection-based mRNA expression microarrays. *Methods in Mouse Atherosclerosis*, 297-308 (2015).

59 Beer, M. *et al.* Laser-capture microdissection of hyperlipidemic/ApoE−/− mouse aorta atherosclerosis. *Laser Capture Microdissection*, 417-428 (2011).

60 Bianchini, M. *et al.* PD-L1 expression on nonclassical monocytes reveals their origin and immunoregulatory function. *Sci Immunol* **4**, doi:10.1126/sciimmunol.aar3054 (2019).

61 Sun, T. *et al.* Tissue clearing approaches in atherosclerosis. *Methods Mol Biol*, In Press (2021).

62 Cai, R. *et al.* Panoptic imaging of transparent mice reveals whole-body neuronal projections and skull-meninges connections. *Nature neuroscience* **22**, 317-327, doi:10.1038/s41593-018-0301-3 (2019).

6263 Costantini, I. *et al.* A versatile clearing agent for multi-modal brain imaging. *Scientific reports* **5**, 1-9 (2015).

64 Jöns, A. & Mettenleiter, T. C. Green fluorescent protein expressed by recombinant pseudorabies virus as an in vivo marker for viral replication. *Journal of virological methods* **66**, 283-292 (1997).

65 Card, J., Whealy, M., Robbins, A., Moore, R. & Enquist, L. Two α-herpesvirus strains are transported differentially in the rodent visual system. *Neuron* **6**, 957-969 (1991).

66 Cano, G., Card, J. P. & Sved, A. F. Dual viral transneuronal tracing of central autonomic circuits involved in the innervation of the two kidneys in rat. *Journal of Comparative Neurology* **471**, 462-481 (2004).

6667 Carnevale, D. *et al.* Loss of EMILIN-1 Enhances Arteriolar Myogenic Tone Through TGF-beta (Transforming Growth Factor-beta)-Dependent Transactivation of EGFR (Epidermal Growth Factor Receptor) and Is Relevant for Hypertension in Mice and Humans. *Arteriosclerosis, thrombosis, and vascular biology* **38**, 2484-2497, doi:10.1161/ATVBAHA.118.311115 (2018).

6768 Carnevale, L. *et al.* Ultrasound-guided catheter implantation improves conscious radiotelemetric blood pressure measurement in mice. *Cardiovascular Research* **117**, 661-662 (2021).
6869 Carnevale, D. *et al.* Placental growth factor regulates cardiac inflammation through the tissue inhibitor of metalloproteinases-3/tumor necrosis factor-α–converting enzyme axis: Crucial role for adaptive cardiac remodeling during cardiac pressure overload. *Circulation* **124**, 1337-1350 (2011).
6970 Da Ros, F. *et al.* Targeting interleukin-1β protects from aortic aneurysms induced by disrupted transforming growth factor β signaling. *Immunity* **47**, 959-973. e959 (2017).
71 Perrotta, M. *et al.* Deoxycorticosterone acetate-salt hypertension activates placental growth factor in the spleen to couple sympathetic drive and immune system activation. *Cardiovascular research* **114**, 456-467 (2018).
72 Burton, P., Gurrin, L. & Sly, P. Extending the simple linear regression model to account for correlated responses: an introduction to generalized estimating equations and multi-level mixed modelling. *Statistics in medicine* **17**, 1261-1291 (1998).

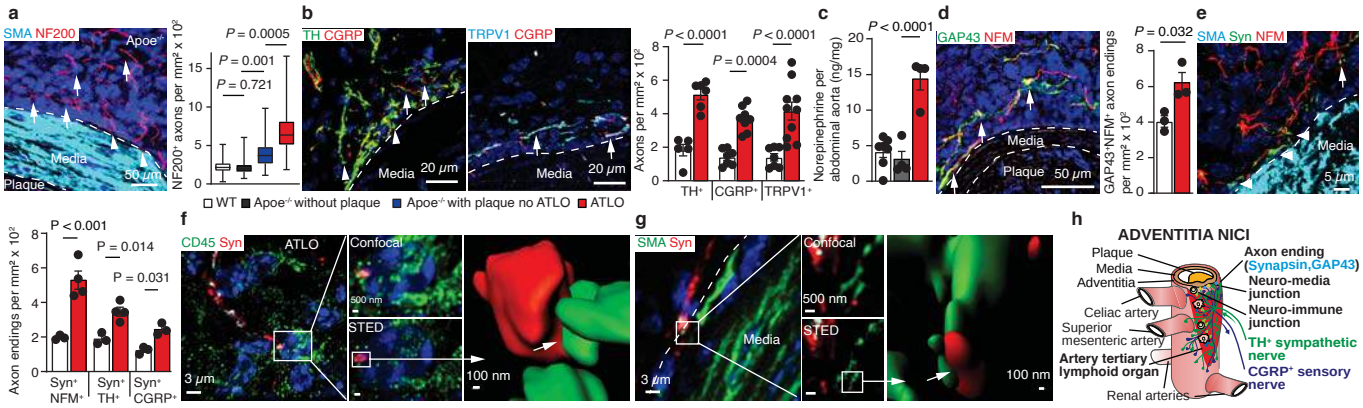
a
SMA NF200
Apoe-/-
Media
Plaque
50 μm
P = 0.0005
P = 0.001
P = 0.721
NF200+ axons per mm² x 10²
b
TH CGRP
TRPV1 CGRP
Media
20 μm
P < 0.0001
P < 0.0001
P = 0.0004
Axons per mm² x 10²
TH+
CGRP+
TRPV1+
c
P < 0.0001
Norepinephrine per abdominal aorta (ng/mg)
d
GAP43 NFM
Media
Plaque
50 μm
e
P = 0.032
GAP43+NFM+ axon endings per mm² x 10²
SMA Syn NFM
Media
5 μm
WT
Apoe-/- without plaque
Apoe-/- with plaque no ATLO
ATLO
P < 0.001
P = 0.014
P = 0.031
Axon endings per mm² x 10²
Syn+ NFM+
Syn+ TH+
Syn+ CGRP+
f
CD45 Syn
ATLO
Confocal
500 nm
STED
100 nm
3 μm
g
SMA Syn
Media
Confocal
500 nm
STED
100 nm
3 μm
h
ADVENTITIA NICI
Plaque
Media
Adventitia
Celiac artery
Superior mesenteric artery
Artery tertiary lymphoid organ
Renal arteries
Axon ending (Synapsin,GAP43)
Neuro-media junction
Neuro-immune junction
TH+ sympathetic nerve
CGRP+ sensory nerve

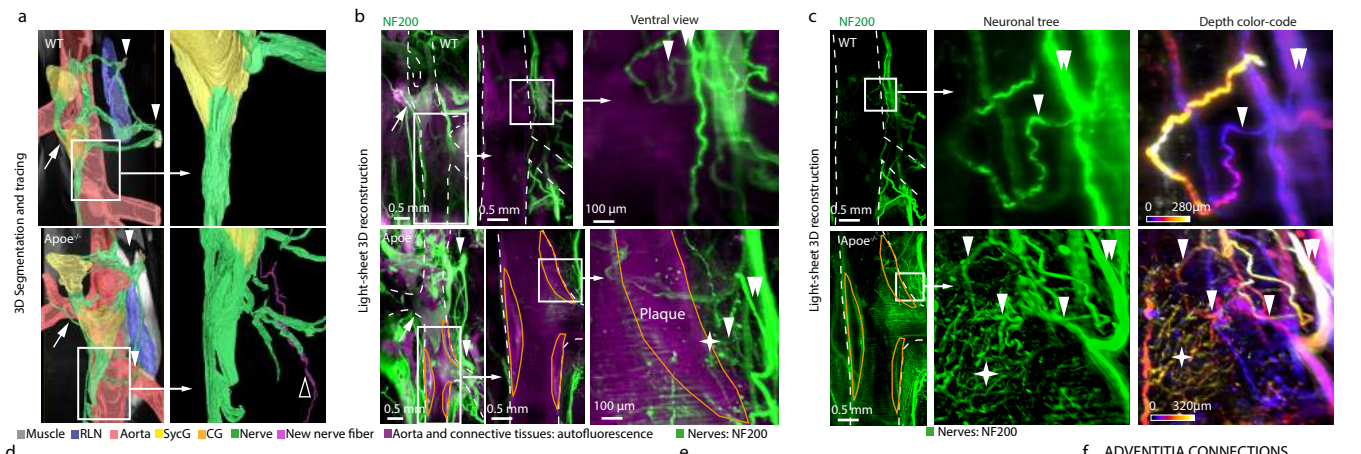
a
WT
Apoe-/-
3D Segmentation and tracing
b
NF200
Ventral view
WT
Apoe-/-
Light-sheet 3D reconstruction
0.5 mm
100 µm
Plaque
c
NF200
Neuronal tree
Depth color-code
WT
Apoe-/-
Light-sheet 3D reconstruction
0.5 mm
0 280µm
0 320µm
Muscle RLN Aorta SycG CG Nerve New nerve fiber
Aorta and connective tissues: autofluorescence
Nerves: NF200
Nerves: NF200

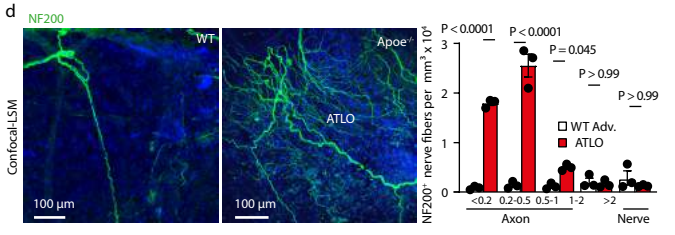
d
NF200
WT
Apoe-/-
ATLO
Confocal-LSM
100 µm
NF200+ nerve fibers per mm² x 10⁴
P < 0.0001
P < 0.0001
P = 0.045
P > 0.99
P > 0.99
WT Adv.
ATLO
<0.2 0.2-0.5 0.5-1 1-2 >2
Axon
Nerve

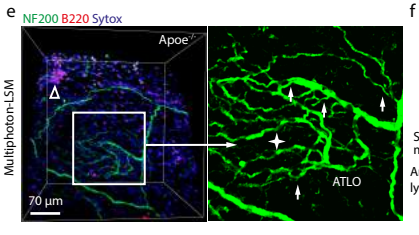
e
NF200 B220 Sytox
Apoe-/-
ATLO
Multiphoton-LSM
70 µm
f
ADVENTITIA CONNECTIONS
Plaque
Media
Adventitia
Celiac artery
Superior mesenteric artery
Artery tertiary lymphoid organ
Renal arteries
Celiac ganglia
Sympathetic chain ganglia

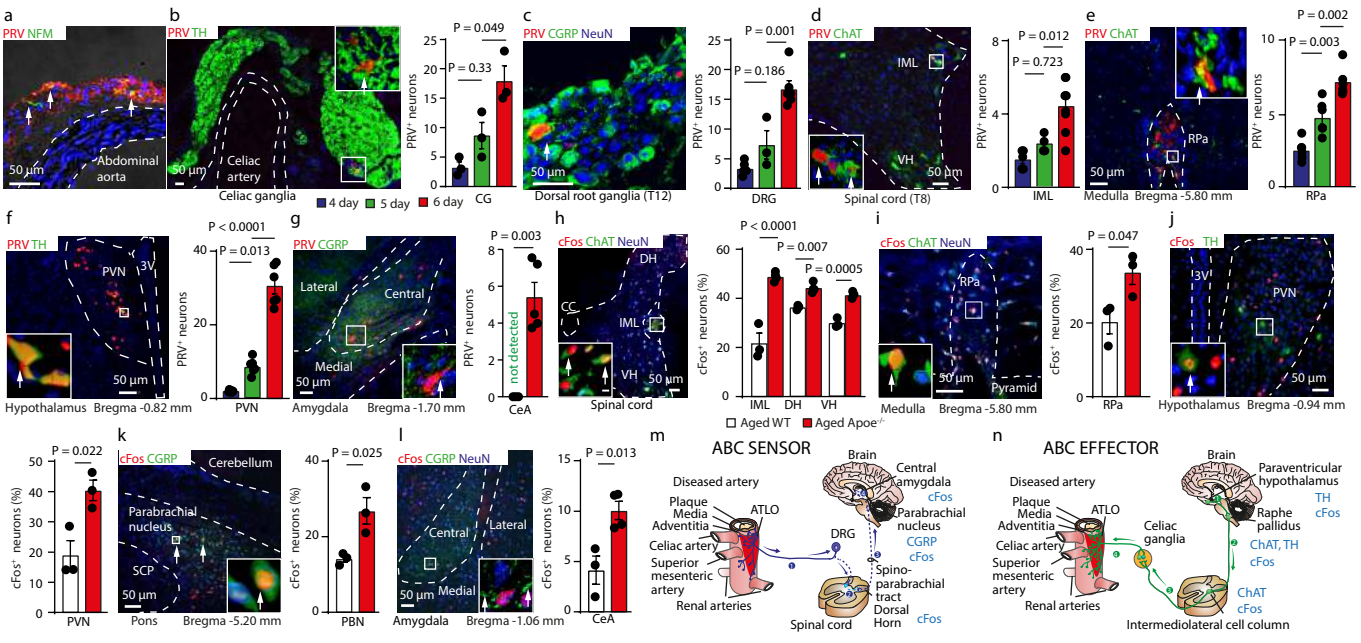
a
PRV NFM
Abdominal aorta
50 µm
b
PRV TH
Celiac artery
Celiac ganglia
50 µm
P = 0.049
P = 0.33
PRV⁺ neurons
4 day
5 day
6 day
CG
c
PRV CGRP NeuN
Dorsal root ganglia (T12)
50 µm
P = 0.001
P = 0.186
DRG
d
PRV ChAT
IML
VH
Spinal cord (T8)
50 µm
P = 0.012
P = 0.723
IML
e
PRV ChAT
RPa
Medulla
Bregma -5.80 mm
50 µm
P = 0.002
P = 0.003
RPa
f
PRV TH
PVN
3V
Hypothalamus
Bregma -0.82 mm
50 µm
P < 0.0001
P = 0.013
PVN
g
PRV CGRP
Lateral
Central
Medial
Amygdala
Bregma -1.70 mm
50 µm
P = 0.003
not detected
CeA
h
cFos ChAT NeuN
DH
CC
IML
VH
Spinal cord
50 µm
P < 0.0001
P = 0.007
P = 0.0005
cFos⁺ neurons (%)
IML
DH
VH
Aged WT
Aged Apoe-/-
i
cFos ChAT NeuN
RPa
Pyramid
Medulla
Bregma -5.80 mm
50 µm
P = 0.047
RPa
j
cFos TH
3V
PVN
Hypothalamus
Bregma -0.94 mm
50 µm
k
P = 0.022
cFos CGRP
Cerebellum
Parabrachial nucleus
SCP
Pons
Bregma -5.20 mm
50 µm
PVN
P = 0.025
PBN
l
cFos CGRP NeuN
Central
Lateral
Medial
Amygdala
Bregma -1.06 mm
50 µm
P = 0.013
CeA
m
ABC SENSOR
Diseased artery
Plaque
Media
Adventitia
Celiac artery
Superior mesenteric artery
Renal arteries
ATLO
DRG
Brain
Central amygdala
cFos
Parabrachial nucleus
CGRP
cFos
Spino-parabrachial tract
Dorsal Horn
cFos
Spinal cord
n
ABC EFFECTOR
Diseased artery
Plaque
Media
Adventitia
Celiac artery
Superior mesenteric artery
Renal arteries
ATLO
Celiac ganglia
Brain
Paraventricular hypothalamus
TH
cFos
Raphe pallidus
ChAT, TH
cFos
ChAT
cFos
Intermediolateral cell column

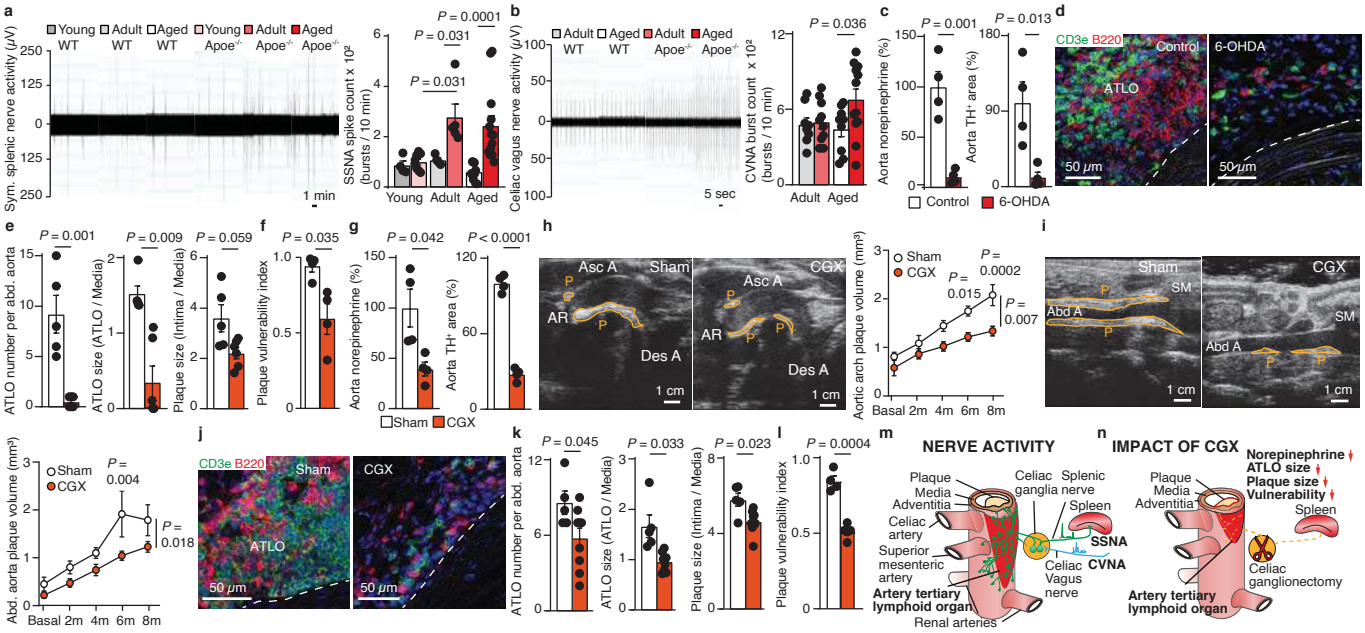
a
Young WT
Adult WT
Aged WT
Young Apoe-/-
Adult Apoe-/-
Aged Apoe-/-
Sym. splenic nerve activity (μV)
1 min
SSNA spike count x 10²
(bursts / 10 min)
P = 0.0001
P = 0.031
P = 0.031
b
Adult WT
Aged WT
Adult Apoe-/-
Aged Apoe-/-
Celiac vagus nerve activity (μV)
5 sec
CVNA burst count x 10²
(bursts / 10 min)
P = 0.036
c
P = 0.001
P = 0.013
Aorta norepinephrine (%)
Aorta TH+ area (%)
Control
6-OHDA
d
CD3e B220
Control
6-OHDA
ATLO
50 μm
e
P = 0.001
P = 0.009
P = 0.059
ATLO number per abd. aorta
ATLO size (ATLO / Media)
Plaque size (Intima / Media)
f
P = 0.035
Plaque vulnerability index
g
P = 0.042
P < 0.0001
Aorta norepinephrine (%)
Aorta TH+ area (%)
Sham
CGX
h
Asc A
Sham
CGX
AR
P
Des A
1 cm
Aortic arch plaque volume (mm³)
P = 0.0002
P = 0.015
P = 0.007
Basal 2m 4m 6m 8m
i
Sham
CGX
SM
Abd A
1 cm
Abd. aorta plaque volume (mm³)
P = 0.004
P = 0.018
j
CD3e B220
Sham
CGX
ATLO
50 μm
k
P = 0.045
P = 0.033
P = 0.023
ATLO number per abd. aorta
ATLO size (ATLO / Media)
Plaque size (Intima / Media)
l
P = 0.0004
Plaque vulnerability index
m
NERVE ACTIVITY
Plaque
Media
Adventitia
Celiac artery
Superior mesenteric artery
Artery tertiary lymphoid organ
Renal arteries
Celiac ganglia
Splenic nerve
Spleen
SSNA
Celiac Vagus nerve
CVNA
n
IMPACT OF CGX
Norepinephrine
ATLO size
Plaque size
Vulnerability
Spleen
Celiac ganglionectomy
Artery tertiary lymphoid organ